ORNL/TM-2023/3088
M3LW-23OR0406013

Comprehensive Characterization of Helium-Induced Degradation of the Friction Stir Weld on Neutron-Irradiated 304L Stainless Steel

W. Tang
M. N. Gussev
T. M. Rosseel
X. Chen

September 2023

OAK RIDGE National Laboratory

ORNL IS MANAGED BY UT-BATTELLE LLC FOR THE US DEPARTMENT OF ENERGY

ORNL/TM-2023/3088
M3LW-23OR0406013

Materials Science and Technology Division
Nuclear Energy and Fuel Cycle Division

COMPREHENSIVE CHARACTERIZATION OF HELIUM-INDUCED DEGRADATION OF THE FRICTION STIR WELD ON NEUTRON-IRRADIATED 304L STAINLESS STEEL

W. Tang
M. N. Gussev
T. Rosseel
X. Chen

September 2023

Prepared under the direction of the
US Department of Energy
Office of Nuclear Energy
Light Water Reactor Sustainability Program
Materials Research Pathway

Prepared by
OAK RIDGE NATIONAL LABORATORY
Oak Ridge, TN 37831-6079
managed by
UT-BATTELLE, LLC
for the
U.S. DEPARTMENT OF ENERGY
under contract DE-AC05-00OR22725

CONTENTS

LIST OF FIGURES

LIST OF TABLES

ABBREVIATIONS

304L SS	304L stainless steel
appm	atom parts per million
BM	base metal
BSE	backscatter electron
DIC	digital image correlation
dpa	displacements per atom
EBSD	electron backscatter diffraction
EDM	electrical discharge machining
FSW	friction stir welding
GB	grain boundary
HAZ	heat affected zone
HFIR	High Flux Isotope Reactor
IMET	Irradiated Material Examination and Testing (facility)
IPF	inverse pole figure
IQ	image quality
KAM	kernel average misorientation
LAMDA	Low Activation Materials Development and Analysis
LWR	light water reactor
LWRS	Light Water Reactor Sustainability (program)
MA	middle advancing side
MR	middle retreating side
MS	middle stir zone
NPP	nuclear power plant
ORNL	Oak Ridge National Laboratory
PCBN	polycrystalline cubic boron Nitride
REDC	Radiochemical Engineering Development Center
rpm	rotation per minute
SE	secondary electron
SEM	scanning electron microscopy
SS	stainless steel
SZ	stir zone
TA	top advancing side
TMAZ	thermomechanical affected zone
TR	top retreating side
TS	top stir zone
UTS	ultimate tensile stress
wppm	weight parts per million
YS	yield stress

EXECUTIVE SUMMARY

The report describes new experimental results on the mechanical performance of the friction stir welds made on neutron-irradiated 304L stainless steel with helium. The report focuses on helium-related issues (e.g., the helium-induced degradation in the welded joint), aiming at the need to repair irradiated components of nuclear power plants. The friction stir welds analyzed here were previously produced at the US Department of Energy's Oak Ridge National Laboratory, and initial characterization work was performed, mostly addressing the microstructure and if macroscopic cracks and helium bubbles present. The present work attempts to perform a more comprehensive study to assess mechanical performance (i.e., microhardness distribution, tensile properties, tensile deformation behaviors, and fractography analysis).

Section 1 briefly describes issues associated with transmutation-induced helium and its effect on weldability, the promising solution for repairing irradiated parts and components using friction stir welding (FSW), and the recent FSW on irradiated 304L stainless steel containing different amounts of helium.

Section 2 describes the studied materials (custom steel heats with ~10 atom parts per million [appm] helium); introduces the FSW tool and parameters; summarizes previous microstructure characterization results, including helium-induced damage (helium bubbles, bubble chains, and microcracks); presents experiments performed in this report (i.e., horizontal and vertical Vickers microhardness test, digital image correlation tensile tests of miniature specimens extracted from the friction stir weld at different metallurgical zones, and fractography analysis of the broken tensile specimens).

Section 3 presents experimental results from microhardness tests, digital image correlation tensile tests, and fractographic analysis; analyzes FSW thermomechanical histories' effects on hardness, tensile properties, and tensile strain distribution; discusses helium-induced damage to friction stir weld mechanical behavior and fracture mechanisms.

Section 4 summarizes the work performed and suggests future work steps, including further characterization of helium-induced damage via in situ tests, thermomechanical affected zone/heat affected zone specimen strain bands and fracture features mechanisms, and reirradiation experiments to investigate the friction stir weld performance in a real nuclear power plant.

1. INTRODUCTION

1.1 ACCUMULATION OF HELIUM IN THE IN-CORE MATERIALS AND ITS EFFECT ON WELDING

Fusion welding is widely used in nuclear power plant (NPP) construction, and common welding techniques, such as gas tungsten arc welding and gas metal arc welding, are routinely employed to weld pristine, nonirradiated materials, providing high-quality joints. However, neutron irradiation and overall harsh in-reactor environments (i.e., temperature, radiation, and mechanical stress fields, elevated pressure, and potential corrosion) compromise material performance. Over time, some parts and components may require repair or replacement that ideally relies on welding techniques. Thus, replacement and repair welding are essential to ensure the long-term viability, competitiveness, and safe lifetime extensions of the existing US reactor fleet.

Fusion repair welding of NPP-irradiated components encounters one specific issue: helium-induced degradation and/or cracking. During nuclear reactor operation, neutron fluxes stimulate transmutation reactions in the NPP structural materials and lead to helium accumulation, mainly because of the transmutation of boron and nickel by the following reactions:

$$^{10}B + n \rightarrow {}^{7}Li + {}^{4}He \quad (1)$$

$$^{58}Ni + n \rightarrow {}^{59}Ni + \gamma \quad (2)$$

$$^{59}Ni + n \rightarrow {}^{56}Fe + {}^{4}He \quad (3)$$

Helium accumulation and helium-related issues are especially severe in water-moderated reactors because of the “soft” neutron spectra with a high fraction of thermal neutrons.

Stainless steels are widely used in nuclear reactors as structural materials. The presence of nickel in stainless steel with boron impurities makes helium accumulation unavoidable. Unfortunately, helium is practically insoluble in steel. The high heat input in fusion repair welding of irradiated stainless steels causes helium to migrate to grain boundaries (GBs) where it tends to form bubbles, drastically embrittling the GB and reducing the GB strength. Moreover, the local transient elevated temperatures during fusion welding result in tensile stresses in the weld and nearby areas that are high enough to initiate crack formation on the helium-compromised GBs and lead to crack propagation in the heat-affected zone (HAZ) and/or weld zone (i.e., helium-induced cracking).

Even 1–3 atom parts per million (appm) of helium is usually enough to cause helium-induced cracking in welding, and austenitic steels with more than 5 appm of helium are often considered nonweldable with current fusion welding techniques. In short, helium accumulates at rates of roughly 0.2–1 appm per displacements per atom (dpa), and 1 dpa usually means about 1 year of service for in-core components. The rates may be an order of magnitude lower for the peripheral components or higher in the core, but, generally, critical helium concentrations (above 1–3 appm) may be reached even for peripheral parts within about 10–20 years. This time is much less than the planned life span of typical NPPs (40 years), even without the extension (usually to 60–80 years). Thus, helium-related issues prohibit fusion welding repair, and such repairs are inevitable during NPP operation.

As an example, in 1986, the gas tungsten arc welding technique was used to repair the water leakage of a Savannah River National Laboratory reactor, and many cracks appeared at the HAZ after repair welding attempts. Those cracks caused the reactor’s permanent shutdown. Investigation showed that these cracks were helium-induced cracks, and helium concentration in the repaired water tank wall was about 3 appm [1]. An example of a fusion weld cross section with helium-induced cracks in the HAZ is shown in Figure

1 [2]; the helium amount was 8.3 appm. Studies have shown that elevated temperatures and the appearance of tensile stress during fusion welding cooling are two key factors in helium-induced crack formation and propagation [3].

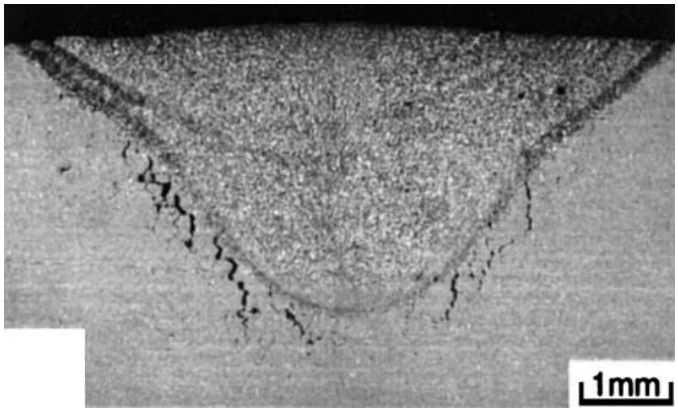

Figure 1. Helium-induced cracks in the weld HAZ of stainless steel containing 8.3 appm helium [2]. Note many cracks exceed 1 mm in length, and the total length of macroscopic cracks is well above ~5–6 mm.

Nickel is a common element in many stainless steels, and boron is an impurity that is difficult to avoid in commercial production; therefore, helium accumulation is unavoidable. At some point, it will reach a critical level to compromise the material's weldability during a reactor's service life.

1.2 FRICTION STIR WELDING AS A PROMISING SOLUTION

Friction stir welding (FSW) is an advanced manufacturing technology [4,5] that involves peak temperatures much lower than the material bulk melting point (generally between 0.6–0.8 T_m). During FSW, the material is heated by friction between the welding tool and welded material as well as by plastic deformation of the material being welded. Heated material flows/deforms around the welding tool, mixing, recrystallization, and forms a joint [6]. Tool wear during high-temperature materials FSW is often mentioned as a minor side effect [7].

In general, a friction stir weld contains four metallurgical zones: stir zone (SZ), thermomechanical affected zone (TMAZ), HAZ, and base metal (BM). The SZ is the material directly affected by the FSW tool. The SZ is usually underneath the FSW tool shoulder and experiences elevated temperature and large plastic deformation. The SZ generally recrystallizes during the cooling process. The TMAZ is located on both sides of the SZ. The TMAZ experiences high temperature and some plastic deformation, but the grain elongation is still seen after the FSW. The HAZ is farther out from the TMAZ. The HAZ receives sufficient thermal input to affect the material microstructure/properties, but no plastic deformation occurs. The BM material microstructure/mechanical properties are not affected by the FSW heat input and plastic deformation. In a friction stir weld cross section, the side where the FSW tool rotates and travels along the same direction is called the advancing side, and the side where the two directions are opposite to each other is called the retreating side.

FSW is arguably the most recent significant invention in welding technologies [6], and it has been widely studied and developed with different materials, from nonferrous metals to ferrous metals [8-10] and from steels to high-alloy materials [11-13]. In many applications, FSW demonstrated outstanding weldability to form high-quality joints. Lower peak temperatures and shorter time at elevated temperature, compared with traditional fusion welding approaches, significantly reduces the intensity of diffusion-based processes, including helium migration. Lower temperatures may also reduce tensile thermal stresses and,

in turn, cracking. These considerations make FSW a potential candidate to weld irradiated material that has high helium content.

1.3 RECENT ACHIEVEMENTS ON IRRADIATED MATERIAL FSW

Although FSW is a promising technique, it had not been used to join irradiated materials until the Oak Ridge National Laboratory (ORNL) team, successfully demonstrated FSW on irradiated 304L stainless steel (304L SS) for the first time at the end of 2017 [6,14,15].

The development of irradiated 304L SS FSW and subsequent initial characterization [6,14] were joint efforts of several organizations, programs, and projects, including ORNL, the US Department of Energy Light Water Reactor Sustainability Program (LWRS), and Electric Power Research Institute (EPRI). Within this effort, the custom 304L SS coupons with different controlled amounts of boron were irradiated at the High Flux Isotope Reactor (HFIR) at ORNL to receive controlled amounts of transmuted helium from boron. The irradiated 304L SS coupons then underwent FSW at ORNL's Radiochemical Engineering Development Center (REDC). FSW was applied on three irradiated 304L SS coupons that contained ~5, ~10, and ~20 weight parts per million (wppm) of boron before irradiation, respectively. Metallographic specimens were removed from all three friction stir welds at ORNL's Irradiated Material Examination and Testing (IMET) Facility [16]. Preliminary characterization on one specimen from each of the friction stir welds, which contained ~10 and ~20 wppm boron prior to irradiation, showed that no macro helium-induced cracking was observed at the weld cross section [6,14-17]. The remaining welded specimens, as well as leftover coupon blocks, are stored at ORNL to support future investigations and current work.

The most recent report of the major characterizations, including helium effects, microstructure characterization, and mechanical properties of irradiated 304L SS friction stir welds can be found elsewhere [17]. The report focused on microstructure conditions, grain size, plastic strain gradients, the morphology of the helium-induced damage, and deformation behavior of the friction stir weld containing ~5.2 appm helium. It also investigated the microstructure and helium-induced damage of the friction stir weld containing ~10 appm helium.

The present report continues the characterization of helium-containing friction stir welds, with a particular focus on microhardness distribution, tensile properties, tensile plastic strain distributions, and helium-induced degradation on the friction stir weld containing ~10 appm helium (20 wppm of boron before irradiation).

2. MATERIALS, EXPERIMENTAL METHODS, AND MAJOR RESULTS OF PREVIOUS CHARACTERIZATION

2.1 CUSTOM 304L STAINLESS STEEL COMPOSITION, FABRICATING, AND PROCESSING

All 304L SS coupons with different levels of boron, including the one characterized in this report (304D-5), were irradiated at HFIR for three operation cycles (22–26 days/cycle) in 2014 [18]. The 304D heat material's chemical composition before irradiation is shown in Table 1. The 304L SS coupon dimensions were 76 × 56 × 8.9 mm. Through fitting tests, 45 stainless steel coupons were placed in the VXF-16, VXF-17, VXF-19, and VXF-21 large bores at HFIR for irradiation. In addition, neutronics calculations using different codes were performed to determine the amount of irradiation required to generate the targeted helium level in each specimen. The irradiation strategy developed was based on completely transmuting boron to helium while minimizing the burning of nickel.

Table 1. Chemical composition of the 304L SS, wt. % [17]

Type	Heat name	B (wppm)	Fe	C	Mn	Si	Cr	Ni	Mo	Cu	N	P	S
Custom B-enriched 304L	304D	24	Bal.	0.01	1.53	0.49	19.33	10.41	0.04	0.05	0.035	<0.001	0.002

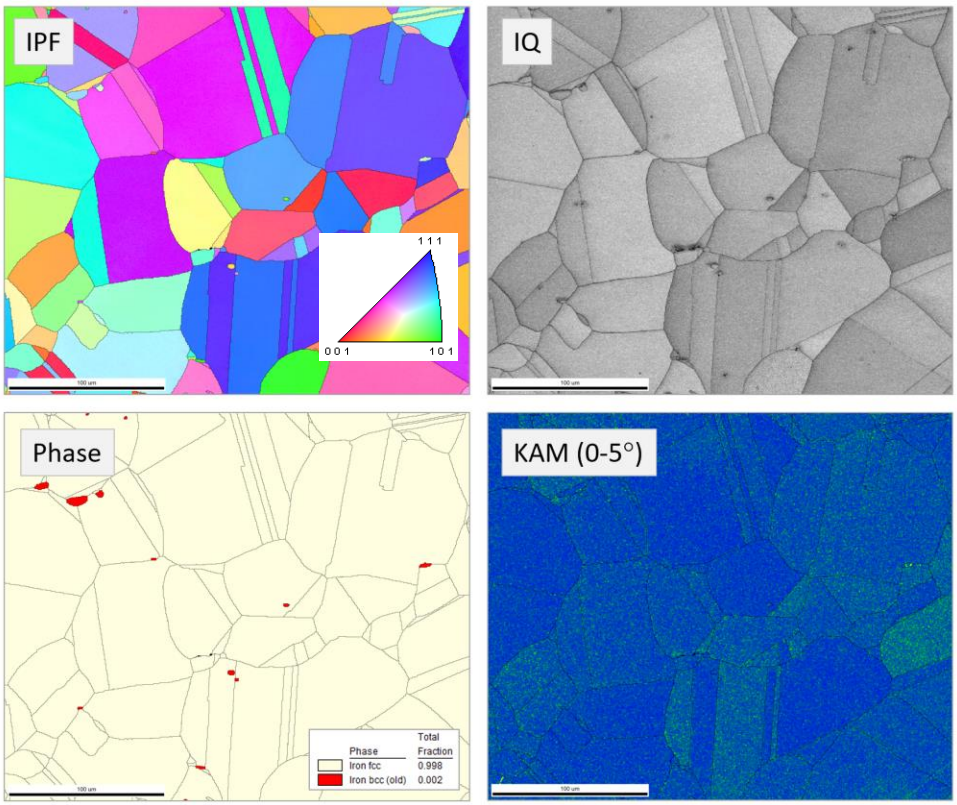

Figure 2. Reference microstructure for 304D custom heat (24 appm boron-enriched, measured ~15.6 appm helium in another coupon with the same heat): electron backscatter diffraction (EBSD) inverse pole figure (IPF), image quality (IQ), phase, and kernel average misorientation (KAM) maps. Visible is the annealed austenite structure with a minor amount of ferrite. Many ferrite grains have a specific elongated shape with a long axis oriented in the horizontal direction. The IQ map shows the reduced pattern quality around many ferritic grains (no such effect was observed in 304C heat); reduced Kikuchi pattern quality may suggest some element segregation effects. The KAM map reveals no plastic strain (fully annealed conditions). Amount of ferrite for this scan <0.2%–0.3%. Scan size: 300 × 250 µm; EBSD step (pitch) size: 0.5 µm.

Figure 2 shows a typical microstructure of the studied materials (304D heat) after the neutron irradiation. The well-annealed austenite structure is visible, along with multiple annealing twins. The analysis showed no pronounced texture in the austenitic matrix. A limited amount of retained ferrite (≪1%) presents in the structure with some insignificant variations between locations and heats; retained ferrite presence is typical for many 300-series steels and is believed to be irrelevant for the present work purposes. Ferrite grains sometimes appeared as bands or chains elongated in one direction—most likely, the former hot rolling direction.

The FSW was performed on the irradiated 304D-5 coupon with an unirradiated 304L SS tab at each end of the irradiated coupon. The irradiated 304L SS coupon dimensions were 76.2 × 55.9 × 8.9 mm, and the tab dimensions were 38.1 × 55.9 × 8.9 mm. A polycrystalline cubic boron nitride (PCBN) tool was used in FSW. The FSW started in the beginning tab, went through the irradiated coupon along the length (55.9 mm) direction, and stopped in the end tab. FSW parameters were 400 rpm and 50.8 mm/min welding speed with position control mode and argon cover gas [14].

After FSW, metallographic specimens (thin slices) were cut from the FSW using a band saw in Cell 6 at the IMET facility. The center of the metallographic specimen was aligned with the center of the friction stir weld, and each metallographic specimen contains SZ, TMAZ, HAZ, and BM. The dimensions of the slices were 30.5 × 8.9 × 2.5 mm. The friction stir weld was located in the middle of the 30.5 mm long slice. The slices were transferred to ORNL's Low Activation Materials Development and Analysis (LAMDA) facility for further preparation and analysis.

The selected thin slice (ID: 304D-5-14), which was cut from the middle section along the friction stir weld length, was epoxy-mounted, mechanically ground, and polished using standard metallography procedures.

2.2 MAJOR RESULTS FROM PREVIOUS SCANNING ELECTRON MICROSCOPY MICROSTRUCTURE CHARACTERIZATION OF THE 304D-5-14 SPECIMEN

The cross section of the friction stir weld is shown in
Figure 3 [17]. The scanning electron microscopy (SEM) image brightness and contrast were adjusted to highlight any potential defects such as cracks and discontinuities in the structure. As expected, macroscopic defects (e.g., approximately millimeter length) should be easy to detect at the given conditions. Image analysis reveals that it is a solid metallic surface without any visible cracks or voids.

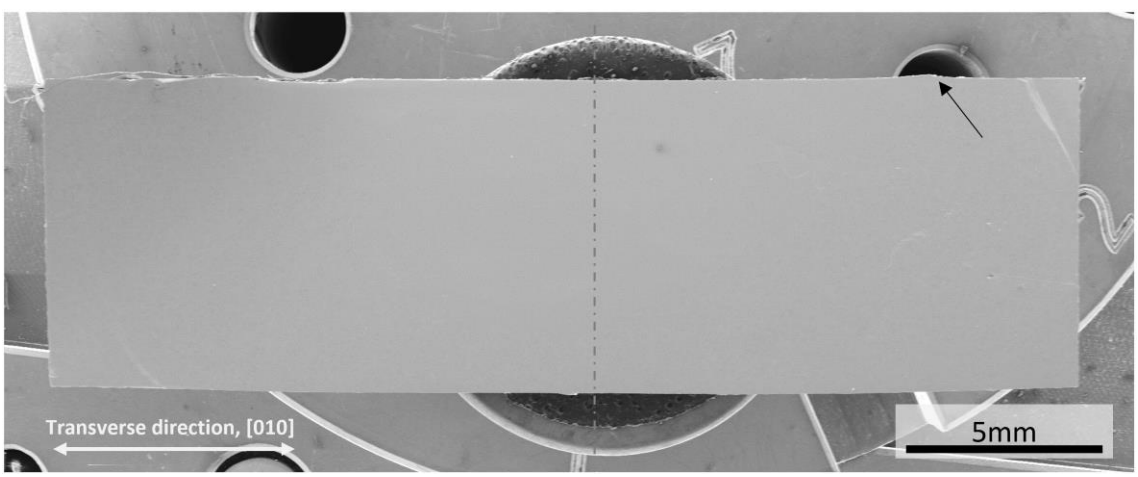

Figure 3. Cross section of the friction stir weld performed on the 304L SS containing ~10 appm helium. No macroscopic cracks or crack-like defects (e.g., ~0.5 mm) were observed in the SZ or TMAZ. The SEM image has some minor distortion because of the low magnification level. Left side: FSW advancing side; right side: FSW retreating side [17]

The absence of etching makes the friction stir weld shape and boundary difficult to visualize. However, the schematic SZ and TMAZ shapes were plotted on the specimen cross section shown in Figure 4 by taking into account some visible features such as the edges of the undercut at the specimen surface and the root tip, the typical shape of a 304L SS friction stir weld made by the same FSW tool, and the SEM observation of the 304L SS friction stir weld specimen.

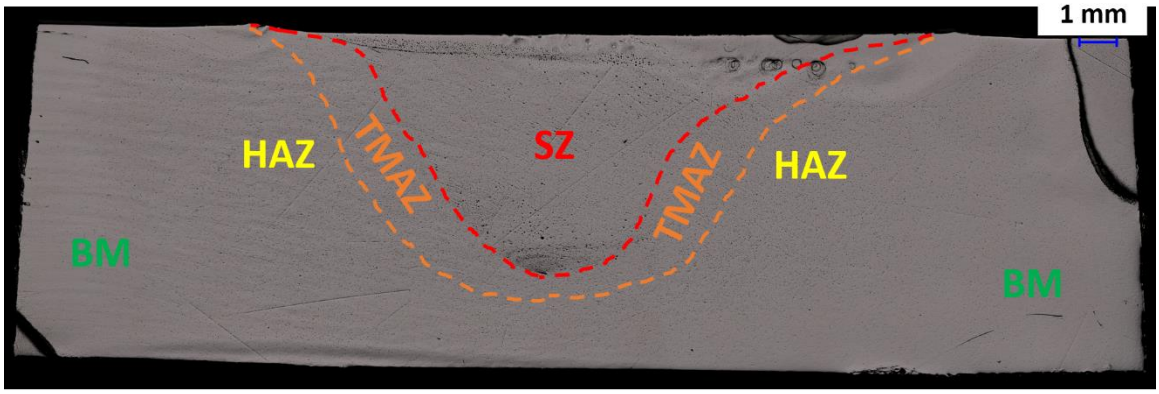

Figure 4. Schematic of the SZ, TMAZ, HAZ, and BM in an irradiated 304L SS friction stir weld.

Typical friction stir weld microstructures were observed in different metallurgical zones of the 304D-5-14 specimen, as shown in Figure 5 [17]. The SZ microstructure (two images on the right) contains roughly shaped, sometimes equiaxed grains, approximately 20–40 µm in size. The SZ area is practically ferrite free because of the experience at elevated temperature during FSW. At the SZ root, grains in the SZ are very fine because of the low heat input in FSW, and grains become much larger in the TMAZ outside of the SZ root (middle bottom). Grain structure transitions (top left image) are clearly shown from the SZ to TMAZ and HAZ. The TMAZ features elongated grain structures without recrystallization or full recrystallization, whereas the HAZ grain shapes and sizes are close to the reference BM. The reference BM (bottom left) exhibits larger grain structures than those in the SZ.

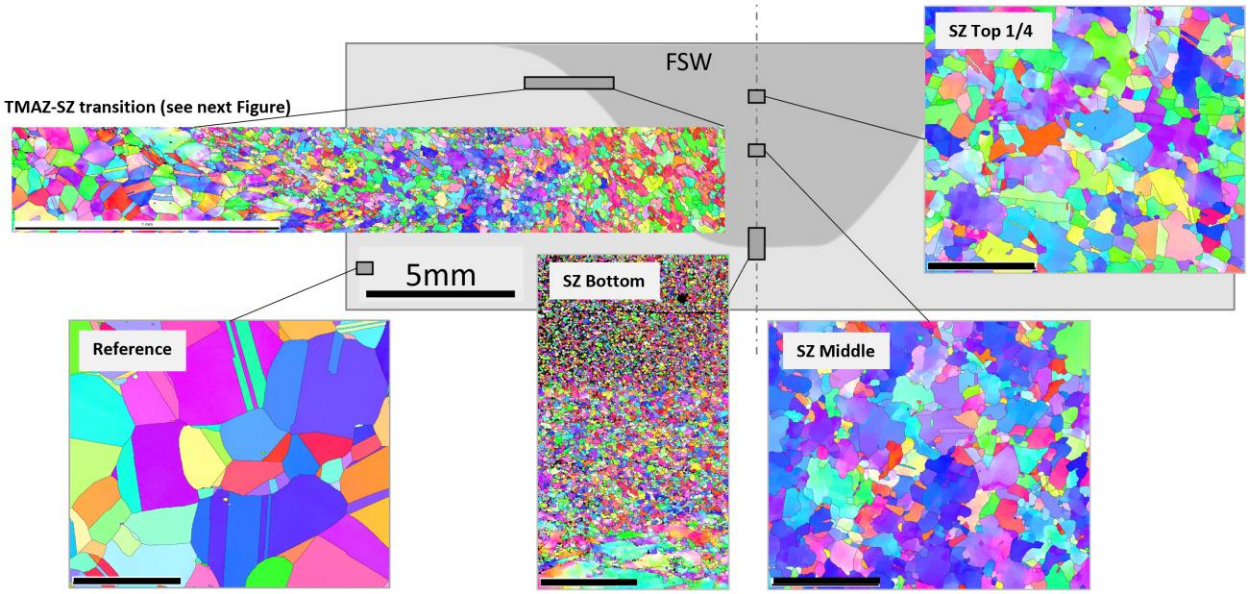

Figure 5. Grain structures in different metallurgical zones of the 304D-5 friction stir weld. The scale bar for grain structure transitions SEM/EBSD image (top left) is 1 mm; for all other images, the scale is 100 µm [17].

Most SEM images inside the 304D-5-14 SZ show specific void-like or bubble-like features (~1–2 µm in size or smaller) of dark color, as shown in Figure 6 [17]. The observed features are round (likely spherical in 3D), and their sizes vary significantly. Their density also varies across the SZ, suggesting their appearance is sensitive to the local conditions. BM location revealed much smaller counts, and the

features presented differently. A significant fraction of the observed round features may be helium bubbles; however, electron energy loss spectroscopy [19] should be used to confirm.

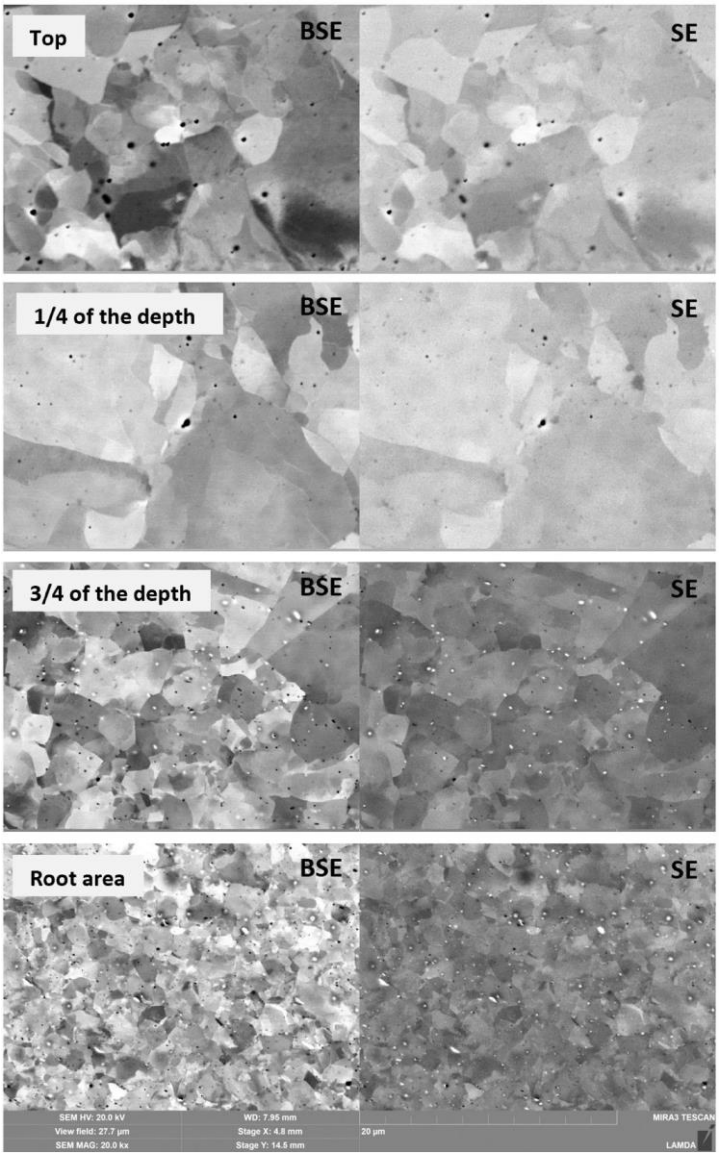

Figure 6. SEM images along the 304D-5-14 SZ centerline [17].

In the TMAZ, individual helium bubbles, helium bubble chains, and several microcracks were observed, as shown in Figure 7 [17]. Individual helium bubbles appear inside grains and on grain boundaries. The helium bubble chains and the microcracks form along grain boundaries. The compromised grain boundaries appear in a small fraction in those pictures, as shown in all images in Figure 7.

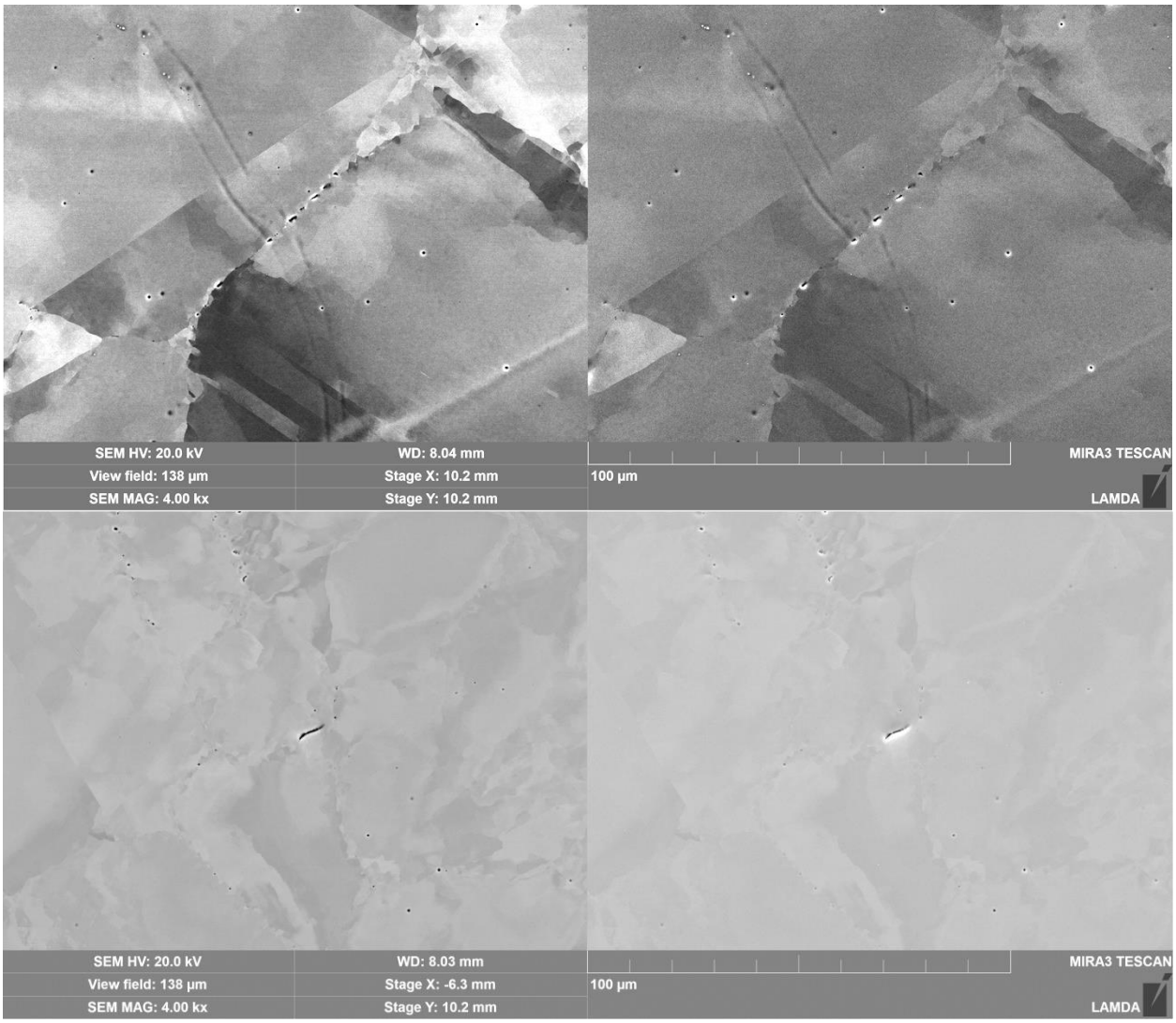

Figure 7. Individual helium bubbles, helium bubble chains, and microcracks in the 304D-5-14 TMAZ [17]. (top) Individual helium bubbles and helium bubble chains in the TMAZ on the 304D-5-14 weld advancing side. (top left) BSE image; (top right) SE image. (bottom) Individual helium bubbles and microcracks in the TMAZ on the 304D-5-14 weld retreating side. (bottom left) BSE image; (bottom right) SE image.

In this 304D-5-14 friction stir weld specimen, helium-induced features often formed specific clusters or "clouds" of large pores and bubbles, as shown in Figure 8 [17]. These clusters are often associated with the retained ferrite grains and preexisting metallurgical inclusions. Such features were not observed in the previously reported friction stir weld with a lower helium content (~5.2 appm).

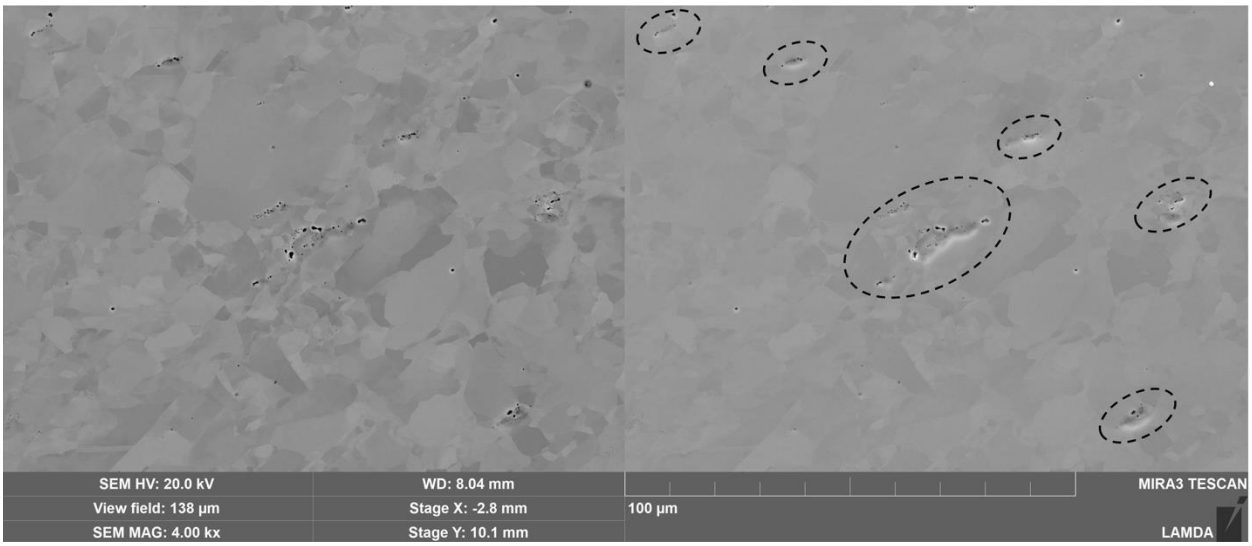

Figure 8. Clustering of the helium-induced damage in TMAZ. Dashed ovals at right show the clusters. (left) BSE image; (right) SE [17].

BM SEM observation revealed larger voids in the 304D-5-14 specimen (~10 appm helium) than in the 304C-5-14 specimen with lower helium content (~5.2 appm). Figure 9 shows the current ~10 appm helium and the ~5.2 appm helium 304L SS BMs under SEM [17]. The helium bubble clusters or clouds in the high-helium-content 304D-5-14 specimen may be caused by the preexisting inhomogeneity of the boron distribution in the base material. Boron segregations (likely elevated boron levels in the retained ferrite and metallurgical inclusions) in turn generated inhomogeneous helium distribution during irradiation in HFIR. Such boron/helium distribution segregations are reflected in the friction stir weld microstructures. However, there could be other reasons caused the helium bubble clusters or clouds, and the boron segregation is just a hypothesis.

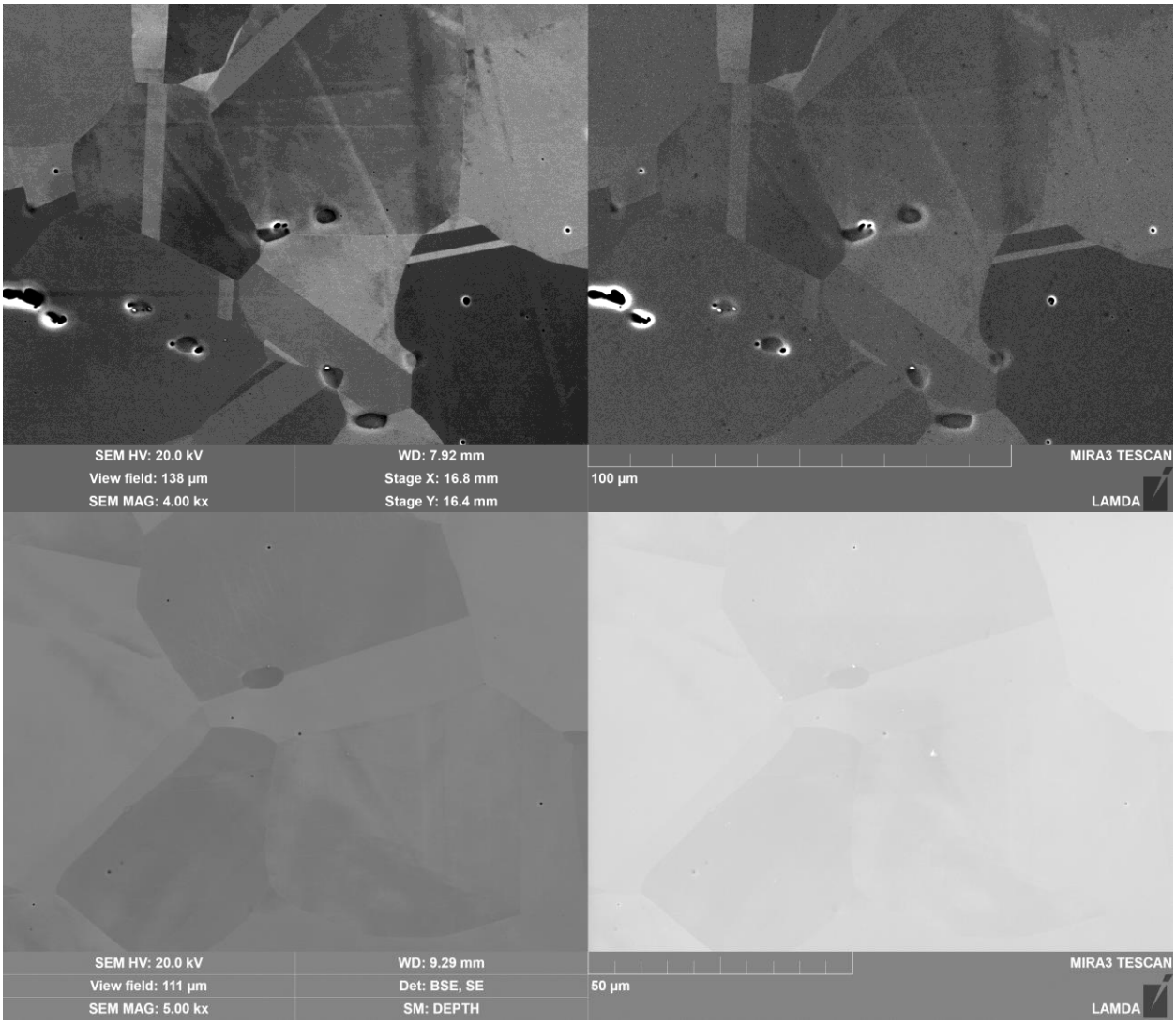

Figure 9. SEM pictures of the 304L SS BMs contains different amount of helium [17]. (top) 304D-5-14 specimen containing ~10 appm helium. (bottom) 304C-5-14 specimen containing ~5.2 appm helium.

2.3 MICROHARDNESS TESTING

Previous SEM characterization identified the friction stir weld shape, location, and boundaries [17]. Vickers microhardness tests were performed on the 304D-5-14 friction stir weld specimen along five horizontal lines and three vertical lines, as shown in Figure 10. The three horizontal lines cross the whole specimen, and they are one-fourth, one-half, and three-fourths of the SZ depth from the weld top surface, respectively. From left to right, the three horizontal lines start at HAZ on the friction stir weld advancing side, go through the TMAZ on the advancing side, the SZ, and the TMAZ on the retreating side, and end at the HAZ on the retreating side. The two short horizontal lines located at the bottom of the specimen left and right corners indicate the BM, and measurements from the two short horizontal lines represent the BM Vickers hardness. The three vertical measurement lines cross the specimen from top to bottom. The middle vertical line goes through the weld root tip, and the other two are on the advancing and retreating sides of the weld, respectively. From top to bottom, the three vertical lines start at the SZ, go through the TMAZ and HAZ, and end at the HAZ. The Vickers microhardness tests were performed using 200 g force, 10 s dwell time, and indentation spacing of 250 µm.

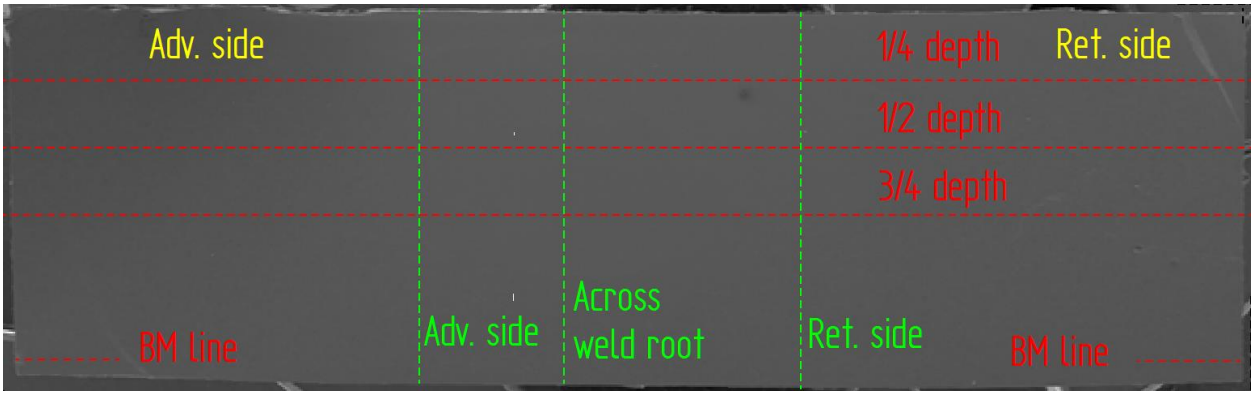

Figure 10. Vickers microhardness measurement lines.

2.4 DIC TENSILE TESTING

The drawing of the miniature tensile specimens used in this study is shown in Figure 11. Such a small specimen can be extracted from different metallurgical zones of the metallographic specimen 304D-5-14. The miniature tensile specimen mapping on the metallographic specimen cross section is shown in Figure 12, which illustrates the long axis of the top row specimens at one-fourth SZ depth, the long axis of the second row of specimens is at five-eighths SZ depth, and the long axis of the bottom specimen is at the SZ root tip. Moreover, specimen gauge areas of the left, middle, and right specimens at the top two rows are located in the TMAZ/HAZ on the advancing side, SZ, and TMAZ/HAZ on the retreating side, respectively. The center of the bottom tensile specimen is at the SZ root tip. The specimen IDs and locations are summarized in Table 2.

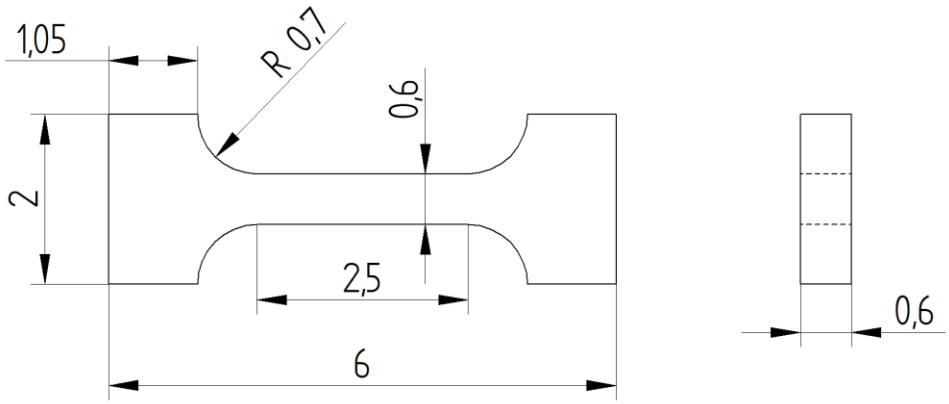

Figure 11. Miniature tensile specimen drawing (unit: mm).

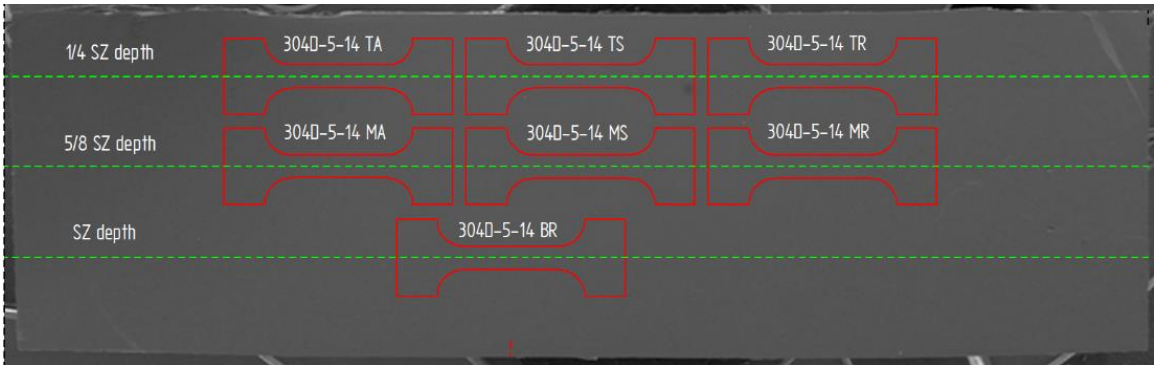

Figure 12. Miniature tensile specimen mapping on the 304D-5-14 friction stir weld specimen.

Table 2. DIC tensile specimen IDs, locations, and gauge area metallurgical zones

Specimen ID	Specimen height location	Gauge area metallurgical zones
304D-5-14 TA	One-fourth SZ depth (top row)	TMAZ/HAZ on the advancing side
304D-5-14 TS		SZ
304D-5-14 TR		TMAZ/HAZ on the retreating side
304D-5-14 MA	Five-eighths SZ depth (middle row)	TMAZ/HAZ on the advancing side
304D-5-14 MS		SZ
304D-5-14 MR		TMAZ/HAZ on the retreating side
304D-5-14 BR	SZ depth (bottom row)	SZ and TMAZ/HAZ on both sides

The mount material was removed from the 304D-5-14 metallographic specimen after microstructure characterization and microhardness tests. Wire electric discharge machining (EDM) was used to extract miniature tensile specimens at different locations, and the wire EDM system in ORNL's LAMDA facility is shown in Figure 13. An extracted miniature tensile specimen is shown in Figure 14.

Figure 13. The wire EDM system installed in LAMDA to manufacture specimens from radioactive material.

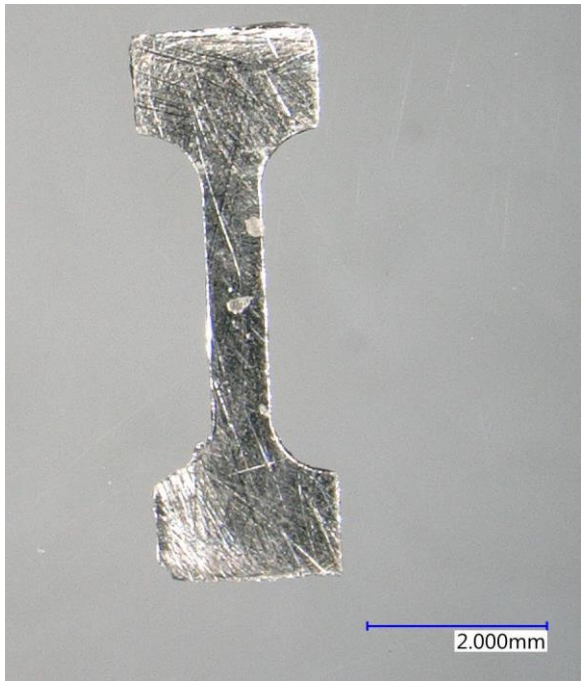

Figure 14. Miniature tensile specimen extracted from the 304D-5-14 friction stir weld metallographic specimen.

After the miniature tensile specimens were extracted, they were cleaned using acetone. Then they were painted with black and white speckle patterns. The MTS Insight 10 tensile frame with a 2.5 kN load cell was used for tensile testing at room temperature at LAMDA. During tensile testing, the specimen surface with painted speckle pattern faced the camera. The tensile strain rate was set to 0.001 s^{-1}, and the image capture rate was 1 s^{-1}.

2.5 FRACTOGRAPHY ANALYSIS

After the mechanical tests, the tensile specimens were cleaned with high-purity acetone and then subjected to an ultrasonic bath in distilled water. This process was repeated at least three times to remove most, if not all, of the paint. Fractographic analysis was performed using a TESCAN MIRA3 SEM. The specimens were mounted on holders inclined at 45°, enabling the analysis of the fracture areas and the tensile portions (at −45° and +45° tilts, respectively). SEM images were captured using a 5 kV voltage and a beam current of approximately 40 pA.

3. RESULTS AND DISCUSSION

3.1 MICROHARDNESS DISTRIBUTIONS

Microhardness distributions of the three horizontal measurement lines across the friction stir weld SZ, TMAZ, and HAZ are shown in Figure 15. The BM hardness (223.5 VHN) is indicated by a straight dashed line, with the average of measured hardness values along the two bottom lines.

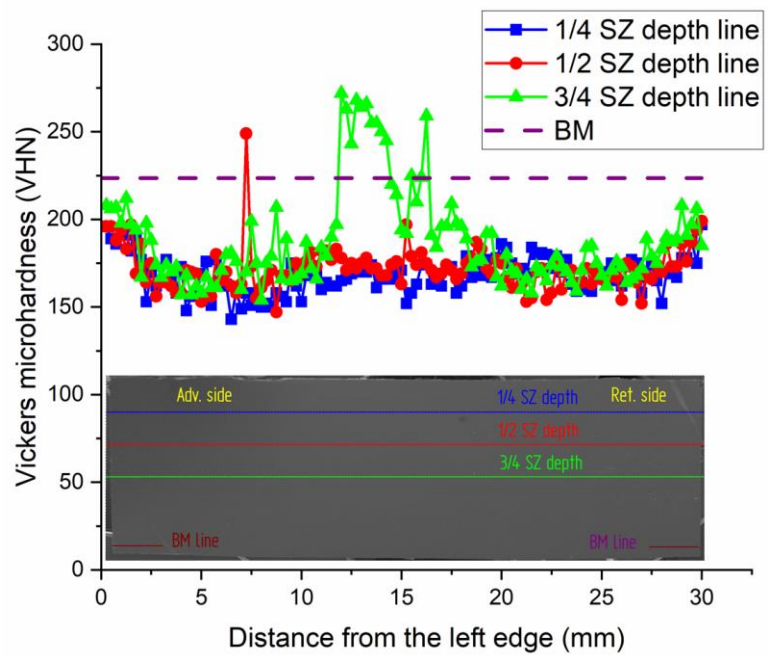

Figure 15. 304D-5-14 friction stir weld specimen horizontal Vickers microhardness distributions.

Hardness values in the SZ, TMAZ, and HAZ measured along the one-fourth and one-half SZ depth were less than that of the BM, and the smallest hardness values were measured in the TMAZ/HAZ area. The hardness values in the SZ and TMAZ/HAZ along the one-half SZ depth line are slightly larger than those along the one-fourth SZ depth line. This difference could be caused by higher peak temperatures and therefore larger grain sizes at locations closer to the tool shoulder (specimen top surface), which generated the most FSW heat input. One hardness value along the one-half SZ depth is obviously larger than the other measurements along the same line and is larger than the BM hardness, but the reason for this apparent outlier remains unknown.

The SZ hardness values along the three-fourths SZ depth measurement line were larger than SZ hardness at higher locations (one-fourth and one-half lines), and some of them were even larger than the BM hardness. The high SZ hardness close to weld root was due to the fine recrystallized grain sizes that resulted from low heat input during FSW (Figure 5). The large variations in SZ hardness along the three-fourths SZ depth line indicated that grain sizes along that line were not uniform because of different thermal and mechanical histories in FSW. By contrast, the TMAZ/HAZ hardness values along the three-fourths SZ depth line were close to or slightly larger than those along the one-fourth and one-half SZ depth lines; these small differences were caused by the different peak temperatures reached in the FSW.

The hardness values and distributions can be modified by adopting different FSW tool designs and by selecting different processing parameters, which mainly control the heat input and plastic deformation in FSW.

Microhardness distributions along the three vertical measurement lines are shown in Figure 16, and the length and width ratio of the picture shown in Figure 16 is changed to fit in the hardness plots. For all three lines' hardness results, measurements close to specimen top (the left edge of the picture) showed SZ hardness, and those close to specimen bottom (the right edge in the picture) indicated HAZ and TMAZ hardness. The SZ middle line stayed in the SZ the longest because it went through the SZ root tip,

whereas the SZ left line was on the advancing side and the SZ right line was on the retreating side of the friction stir weld.

From Figure 16, hardness increased at locations within 1–1.25 mm from the specimen top, where fine grain structures caused by excessive plastic deformation by the FSW tool shoulder were observed. Except for one measurement at this area, the SZ left and SZ right line hardness values are all smaller than that of the BM, regardless of whether the measurement was in the SZ, TMAZ, or HAZ. Furthermore, hardness values from close to the bottom started to increase toward the BM value, which meant the measuring was moving close to the FSW unaffected BM zone. For SZ middle line hardness distribution, in addition to the hardness increase near the top, significant hardness increases occurred at locations 5–7 mm away from the specimen top. These hardness increases (peak value 288 VHN) were caused by the extremely fine grain structures at the weld root area presented in Figure 5.

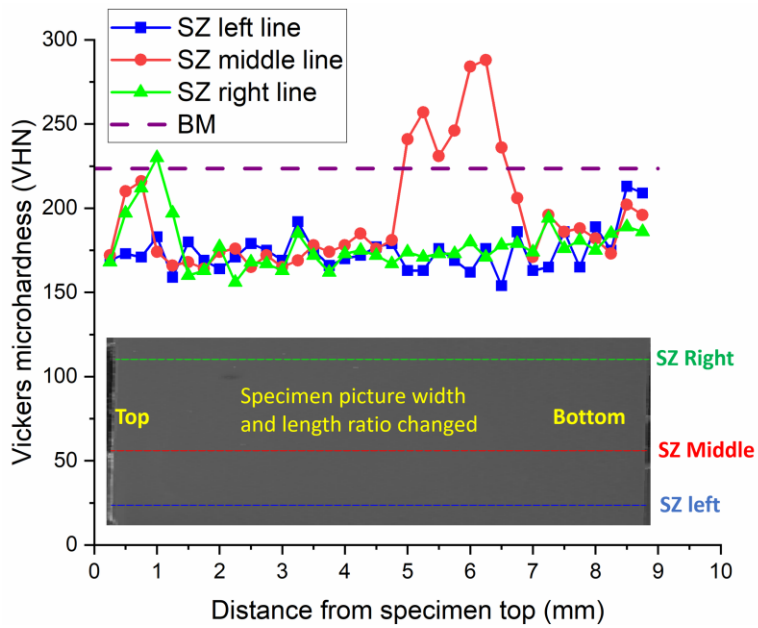

Figure 16. 304D-5-14 friction stir weld specimen vertical Vickers microhardness distributions.

Overall, the microhardness distributions of the 304D-5-14 specimen corresponded with the microstructure observations [17]. Larger hardness values were measured at the top and at the weld root of the SZ, where fine grain structures were observed. In addition, the three-fourths SZ depth horizontal line was about 5.25 mm from the specimen top surface with the hardness increase in the SZ, which agreed with the vertical SZ middle line hardness results (i.e., significant hardness increasing at locations 5–7 mm from the top). Therefore, with the current FSW tool and parameters, the bottom one-fourth SZ area exhibited large hardness values as a result of the thermomechanical effects in FSW.

3.2 TENSILE PROPERTIES AND LOCAL PLASTIC DEFORMATION

Hundreds of images were taken at different load/stress levels during each DIC tensile test. Images with a speckle pattern of miniature tensile specimen 304D-5-14 MS (five-eighths SZ depth in the SZ) at the moment before testing, at the tensile load of ultimate tensile strength (UTS) stress, and right before specimen failure are shown in Figure 17. As shown in the images, the specimen experienced significant deformation/elongation during the tensile test, and exhibited obvious necking before it broke, indicating good ductility in the SZ.

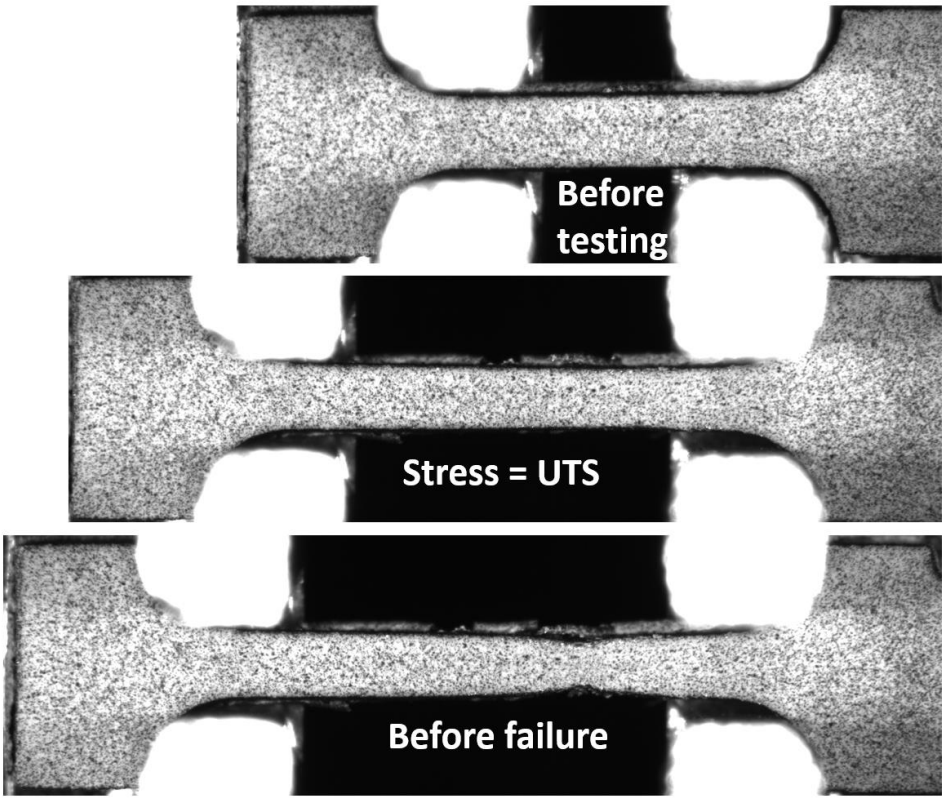

Figure 17. 304D-5-14 MS images. (top) Before testing, (middle) at UTS, and (bottom) before failure.

A 2.5 mm line was applied in the gauge area on the first image of each specimen as the digital extensometer. With the software processing, the length of the digital extensometer could be calculated for every image taken in the tensile test. Therefore, elongations, obtained from the initial digital extensometer length and its changes during the test, can be obtained at corresponding stress levels. The initial extensometer (red line in the specimen gauge area) and appearances at UTS and right before the failure of the 304D-5-14 MS specimen are shown in Figure 18. Clearly, the digital extensometer had large extension before the specimen fail.

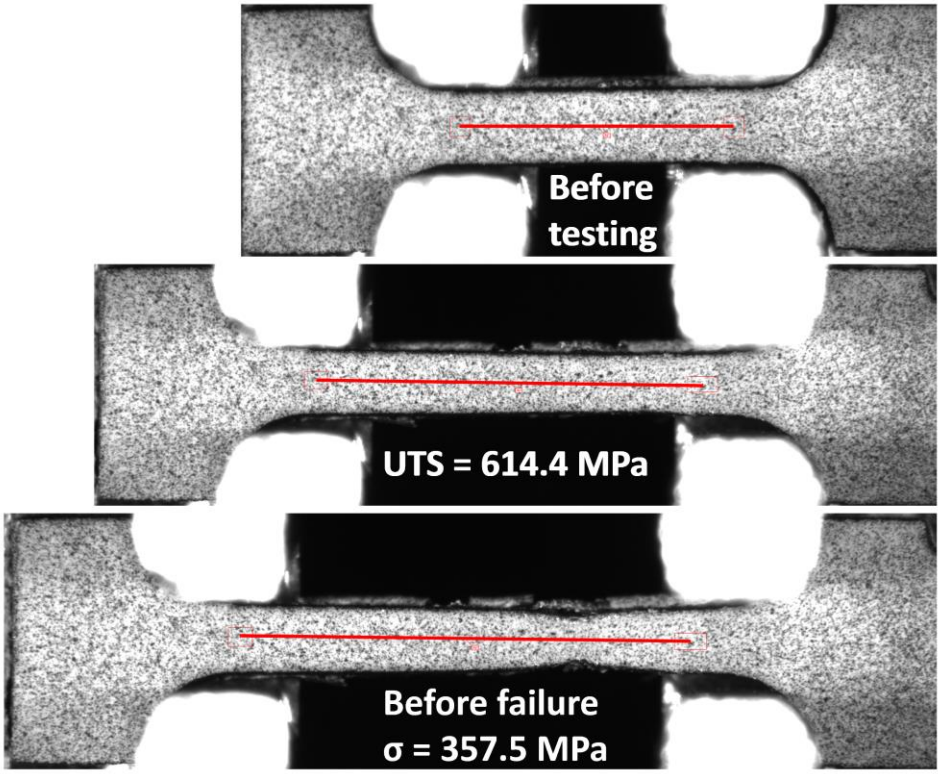

Figure 18. 304D-5-14 MS images with digital extensometer. (top) Before testing, (middle) at UTS, and (bottom) before specimen failure.

By correlating elongations obtained from the digital extensometer and recorded tensile stresses, the tensile curves and tensile properties were obtained. All tensile curves and tensile properties of the seven miniature tensile specimens are shown in Figure 19 and listed in Table 3. Despite helium bubbles in the SZ (Figure 6) and helium bubbles, bubble chains, and microcracks in the TMAZ (Figure 7), all tested specimens exhibited higher yield strength and ultimate tensile strength than ASTM minimum strength requirements of wrought 304L SS (170 MPa yield strength and 485 MPa ultimate tensile strength) [20]. Except for the specimen at the weld root (304D-5-14 BR), all specimen elongations were also higher than the ASTM minimum elongation requirement of wrought 304L SS elongation (40%) [20]. Furthermore, the extensometer length for the current experiment (2.5 mm long) is very different from that of conventional 304L SS (50 mm long). The BM tensile elongation of the irradiated 304L SS with ~5.2 appm helium was 71.3% [21]. Moreover, the uniform elongation of each tensile curve possessed a large ratio of total elongation, indicating excellent ability to remain in uniform deformation and resist necking and rapid fracture propagation. The smallest elongation (32.1%) was measured from the specimen extracted at the weld root, which also presented the highest yield strength and ultimate tensile strength. Such relatively high strength and low elongation properties were results of the superfine grain sizes in the SZ root, which caused dislocation movement difficulty in the SZ and strain localization in the TMAZ during the tensile process.

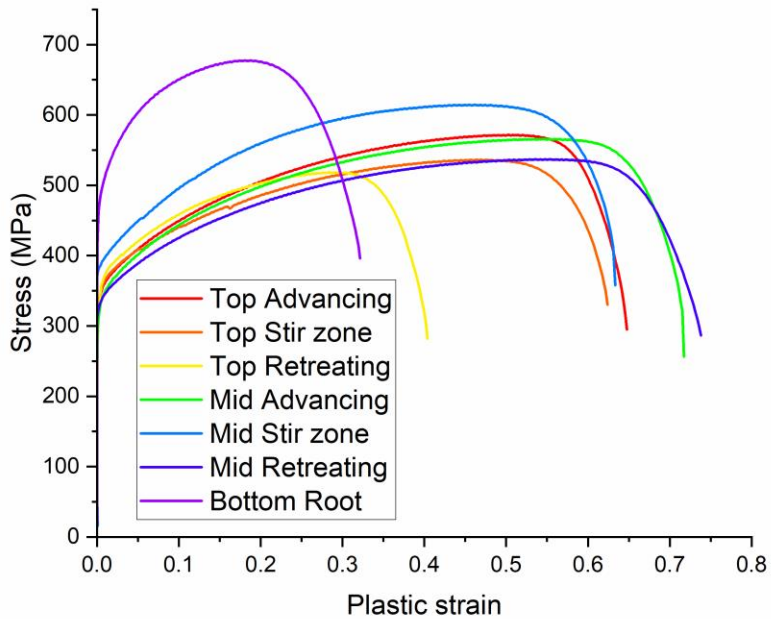

Figure 19. 304D-5-14 tensile curves of all friction stir weld miniature tensile specimens.

Table 3. 304D-5-14 friction stir weld specimen tensile properties.

Specimen ID	Yield strength, MPa	Ultimate tensile strength, MPa	Uniform elongation, %	Total elongation, %
304D-5-14 TA	329.3	571.7	51.5	64.8
304D-5-14 TS	327.9	536.3	46.9	62.4
304D-5-14 TR	320.3	518.4	30.3	43.3
304D-5-14 MA	312.2	565.7	56.6	71.8
304D-5-14 MS	380.6	614.4	47.5	63.3
304D-5-14 MR	323.7	536.9	55.4	73.8
304D-5-14 BR	462.6	677.5	18.2	32.1

Therefore, although helium bubbles, helium bubbles chains, and a few microcracks were present in the SZ, TMAZ, and HAZ, they did not cause catastrophic effects on the friction stir weld strength and ductility.

By applying 2D analysis on the DIC results, local strain distributions and changes in the specimen gauge area were obtained.

The 304D-5-14 MS specimen (middle stir zone) strain ε_x (strain along the pulling direction) distributions at different tensile stages, including global yield, uniform deformation, UTS, and necking, are shown in Figure 20. The green dashed lines in the tensile curve plot illustrate corresponding tensile stages of the strain distribution images. Figure 20 indicates that plastic strains were mainly within the specimen gauge area after yielding, and the peak strains (red) were distributed at the right half of the gauge area. After the

tensile stress reached UTS, plastic strain localized in a small area of the previous wide peak strain zone, and the specimen broke at the same location by the end of tensile test.

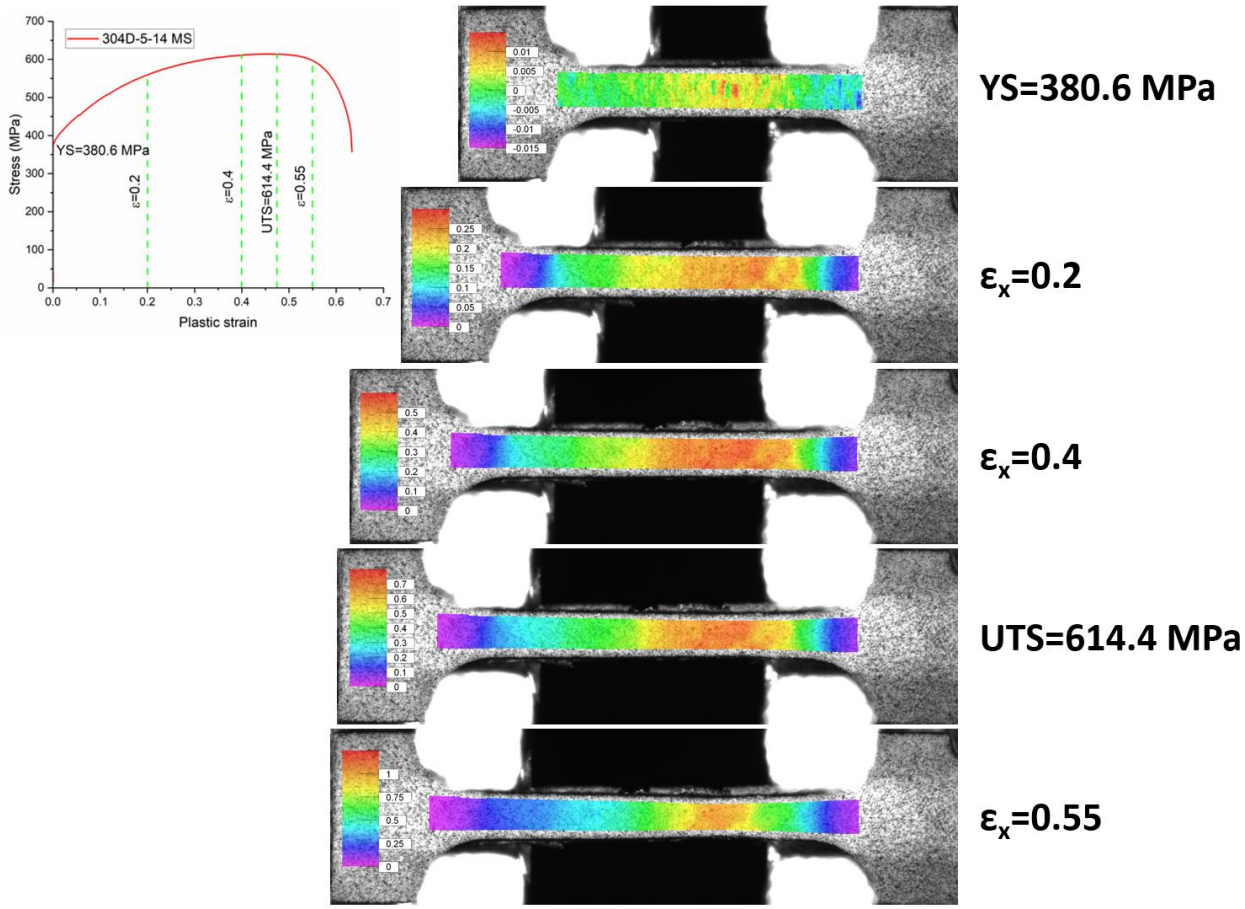

Figure 20. Local strain ε_x distribution of 304D-5-14 MS specimen at different tensile stages.

The bottom root specimen 304D-5-14 BR strain ε_x 2D distributions at different tensile stages, including at yield, between yield and UTS, at UTS, and during necking, are shown in Figure 21. For the 304D-5-14 BR specimen, strain localization occurred shortly after the tensile stress reached yield and before it reached UTS because of the inhomogeneous microstructures and hardness distributions at the SZ root area. Inside the SZ root, grains are superfine with high hardness, but grains became much larger in the TMAZ right outside of the SZ root with low hardness (Figure 4, Figure 15, and Figure 16). Therefore, in the tensile test, plastic deformation was localized at the softer TMAZ soon after the tensile stress reached yield stress (YS), and specimen failed at the same location by the end of the test.

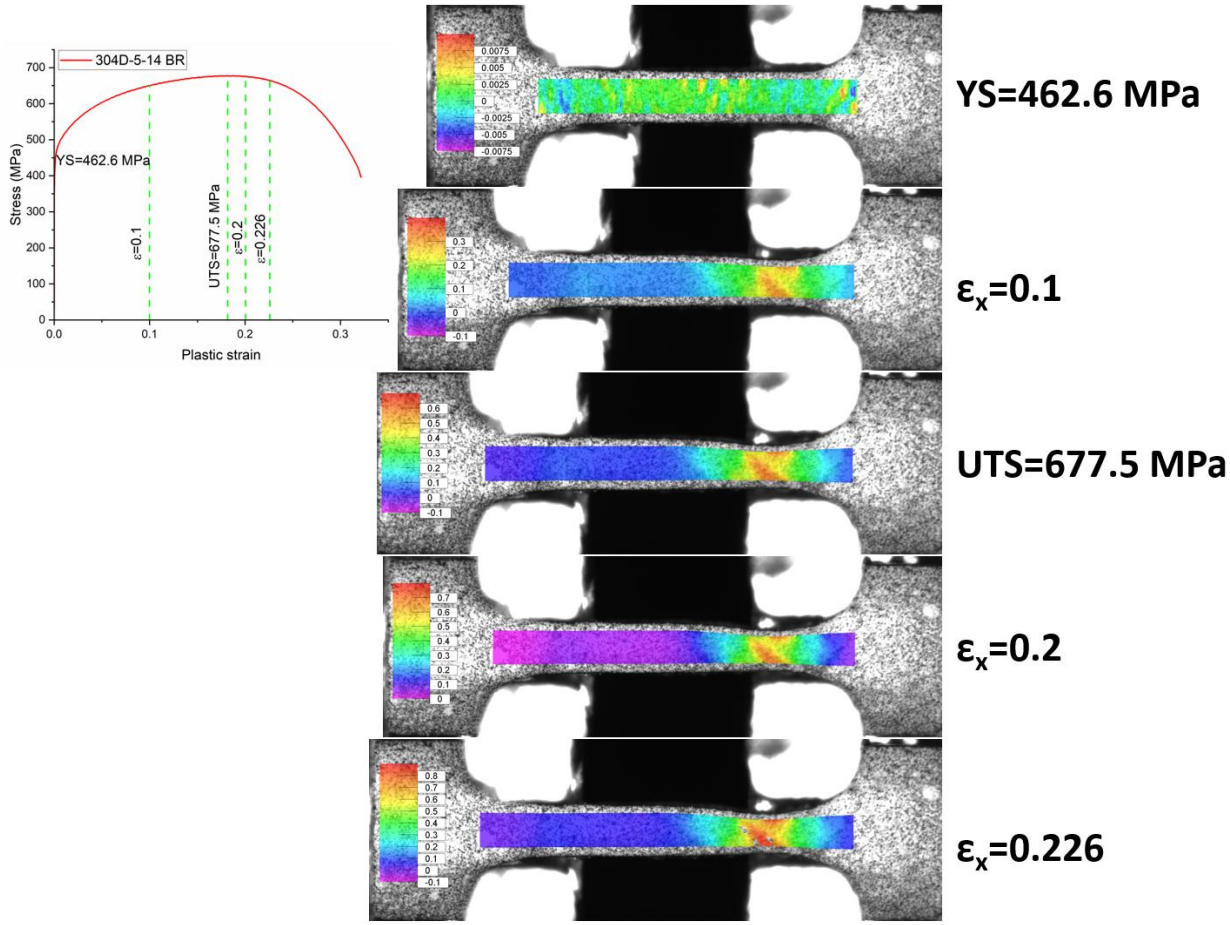

Figure 21. Local strain ε_x distribution of 304D-5-14 BR specimen at different tensile stages.

The strain ε_x distributions of the TMAZ/HAZ specimens at the top advancing side and the middle retreating side are shown in Figure 22 and Figure 23, respectively. Unlike the relatively uniform strain distribution of the SZ specimen (Figure 20) and the early stain localization of the bottom root specimen (Figure 21), multiple plastic strain bands, about 45° from the specimen gauge length directions, were present soon after the TMAZ/HAZ specimens yielded. Tensile strains inside the strain bands are much larger than those outside the strain band, although they might be within the same metallurgical zone. Those strain bands continue to exist when tensile stresses were between YS and UTS, and some strain bands even presented when the stresses reached UTS with strains larger than 0.5 in Figure 22 and Figure 23. At the UTS, the strain band widths were about 60–120 μm for both specimens. Further studies are needed to identify the mechanism of the strain bands present, which could be related to the FSW thermal and mechanical histories in the TMAZ and HAZ, the FSW tool-determined TMAZ and HAZ geometry, and/or irradiation effects such as helium aggregation.

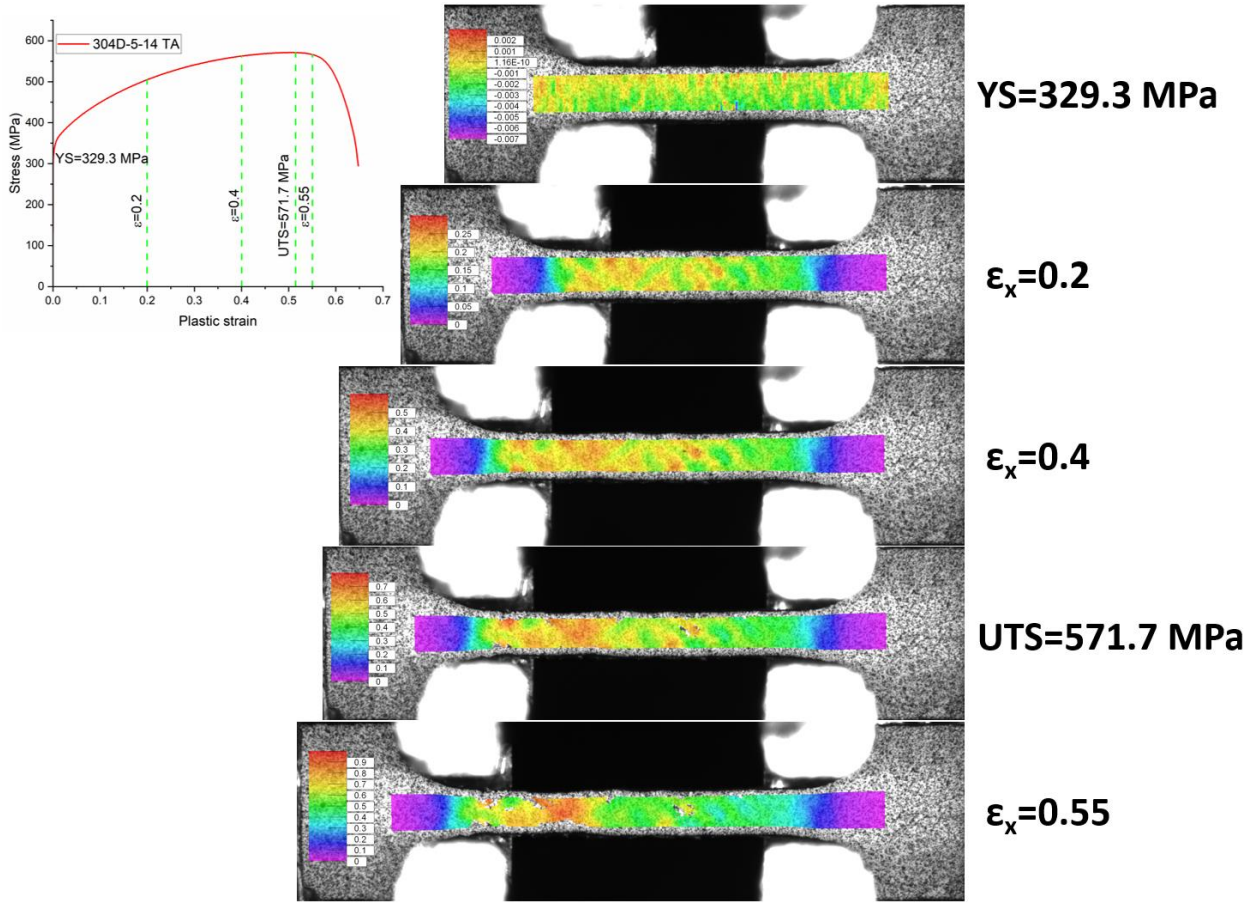

Figure 22. Local strain ε_x distribution of 304D-5-14 TA specimen at different tensile stages.

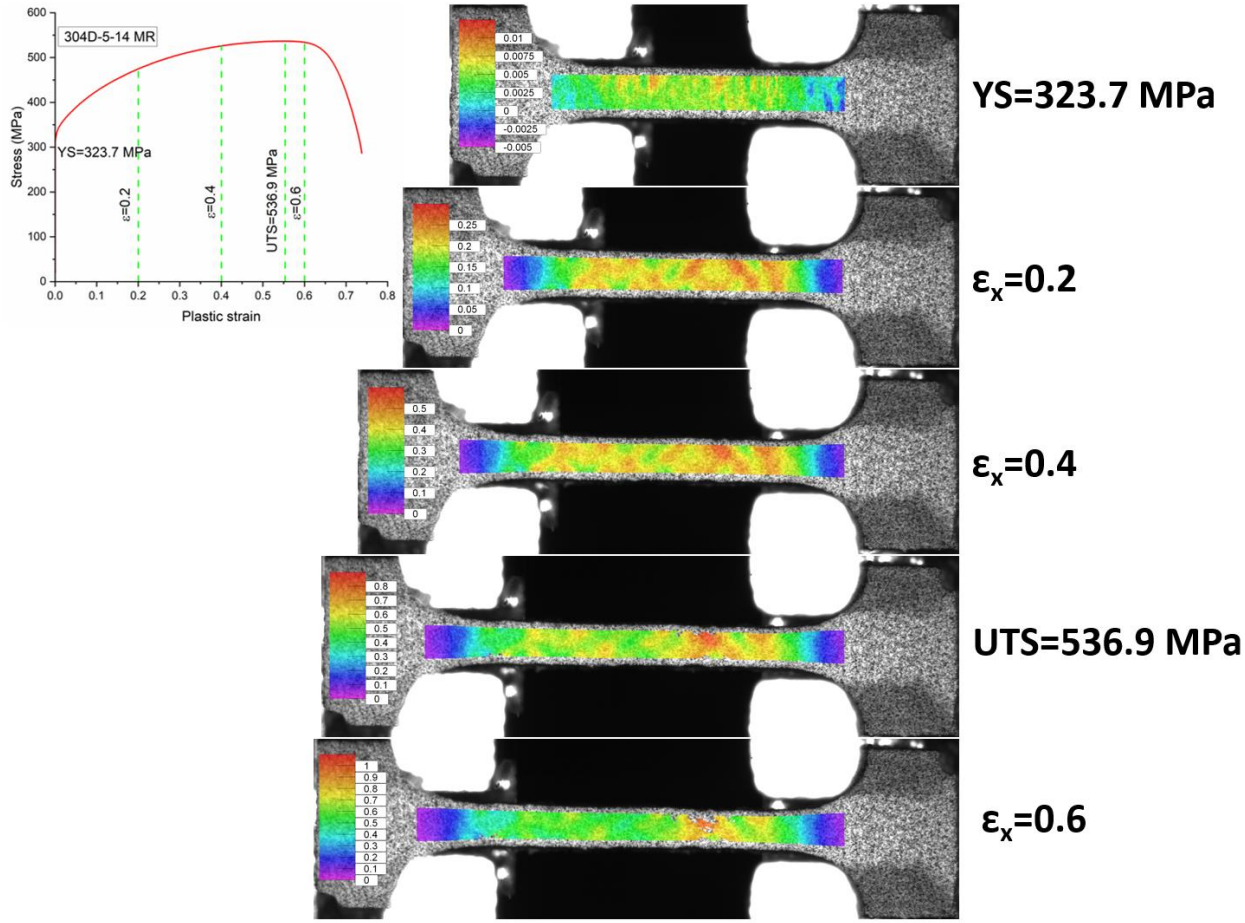

Figure 23. Local strain ε_x distribution of 304D-5-14 MR specimen at different tensile stages.

3.3 FRACTORGRAPHY ANALYSIS

3.3.1 Analysis of the specimen fracture area

Figure 24 provides an overview of the fracture surface for all tested specimens. In most of the specimens, the fracture area assumes a square-like shape with dimensions roughly measuring 300 ×y 300 µm. This significantly smaller cross-sectional area (300 ×y 300 µm compared with approximately 600 × 600 µm in Figure 11) and the consequent high area reduction imply the high ductility of the friction stir welded material. The fracture surface predominantly exhibits signs of ductile fracture, evident from the ductile dimples (covering the majority of the surface) or ductile shear (occupying a smaller region). Certain features, not associated with ductile fracture (e.g., deep holes, pores, and crack-like structures, highlighted by black arrows in Figure 24), were also observed. However, their frequency and overall surface area coverage were minimal, typically one or two per specimen, with the notable exception of the TR specimen, as shown in Figure 24a. The TR specimen exhibited several crack-like features.

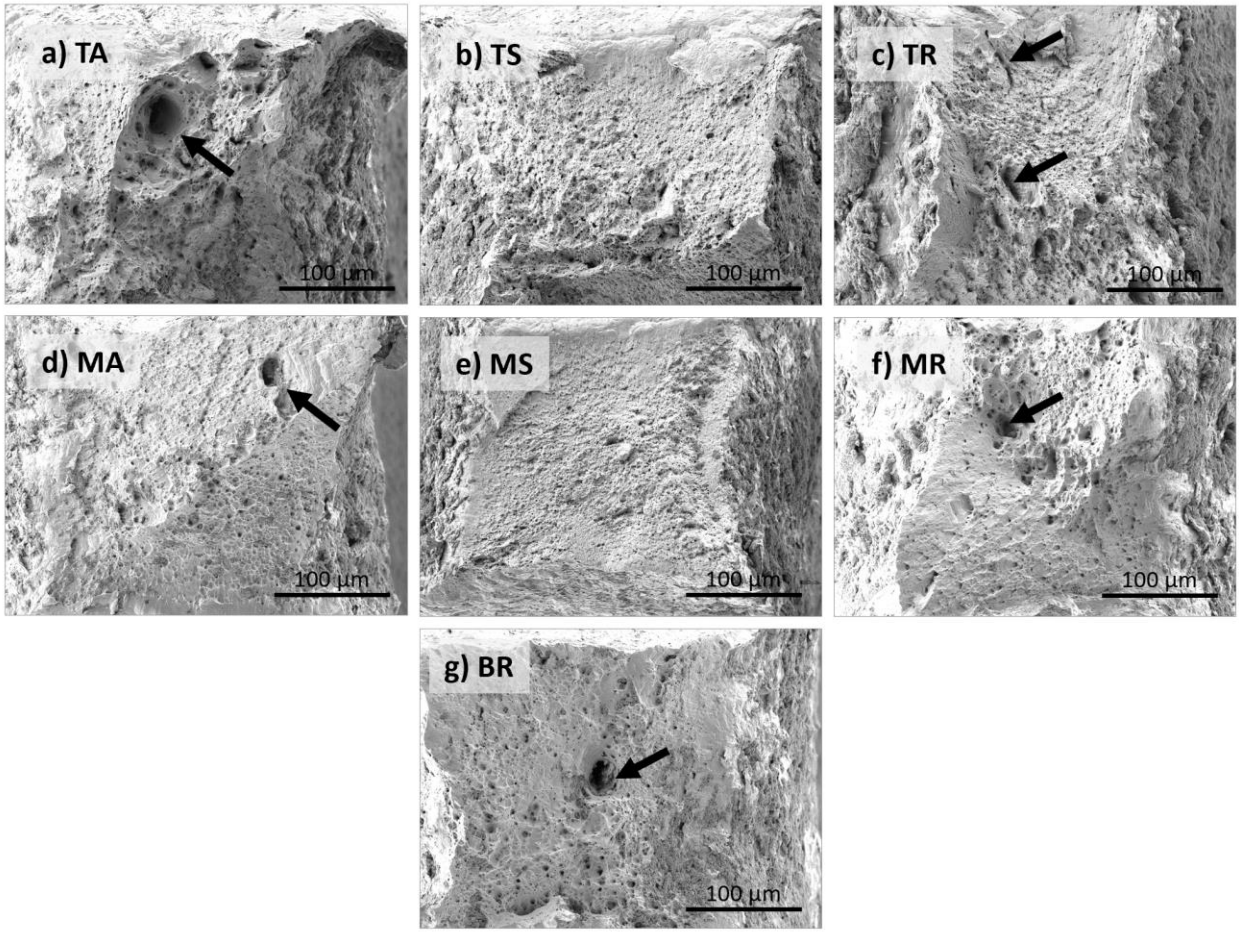

Figure 24. Low-magnification (800×) SEM images of the fracture regions of the tested tensile specimens. Material condition IDs and image order (e.g., "TA") correspond to Figure 12 and Table 2. The dominating ductile fracture is visible, and minor features (indicated by black arrows) are likely related to boron-rich regions.

Figure 25 provides a detail view of the typical fracture surface. The dominant features are ductile dimples, which slightly vary in size based on different metallurgical locations. Although ductile dimples or ductile shear predominantly characterize the TR specimen (as shown in Figure 25c), evidence of ductile tearing is intertwined with features that are believed to be related to the initiation and growth of internal cracks (indicated by the black arrow in Figure 25c).

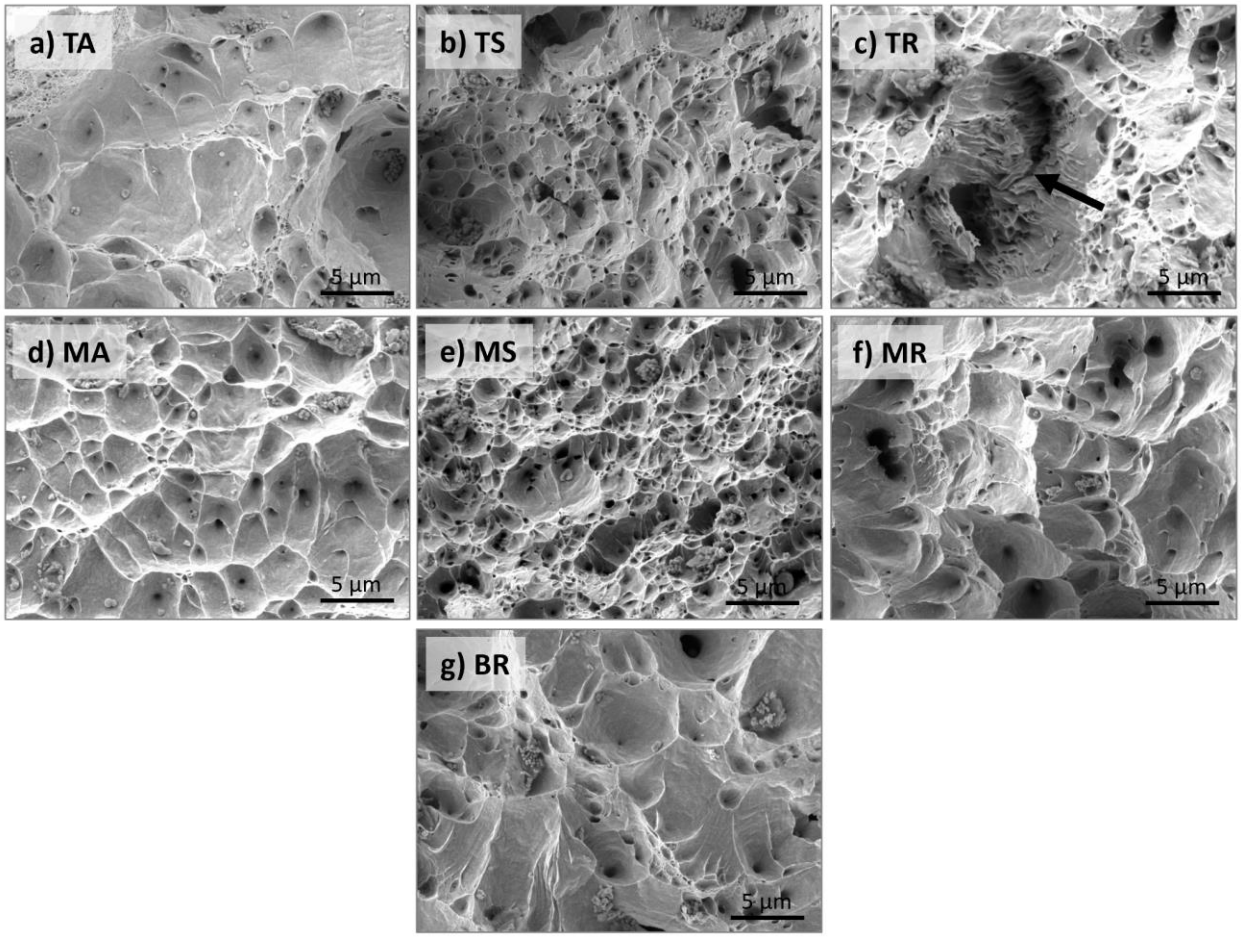

Figure 25. High-magnification (nominal magnification 10,000×) SEM images of typical fracture surface appearance. Material condition IDs are listed in Figure 12 and Table 2.

3.3.2 Helium-related features

Figure 26 displays features that are believed to be related to the presence of helium (boron)-rich regions and compromised grain boundaries. The most commonly observed features are deep, trench-like structures formed at compromised boundaries containing chains of helium bubbles, as depicted in Figure 26(a, b, c). The deep holes shown in Figure 26(d, e) potentially indicate coarse inclusions or large helium bubbles. The unique "ductile bridges" or "pillars" shown in Figure 26f underscore the intricate geometry of the internal damage. Minor cleavage areas, as shown in Figure 26g, likely correspond to helium-rich zones. Deep localized fractures, presented in Figure 26h, are relatively infrequent and are presumably due to metallurgical inclusions. In all cases, except for the TR specimen, such features constitute only a minor portion of the observed area.

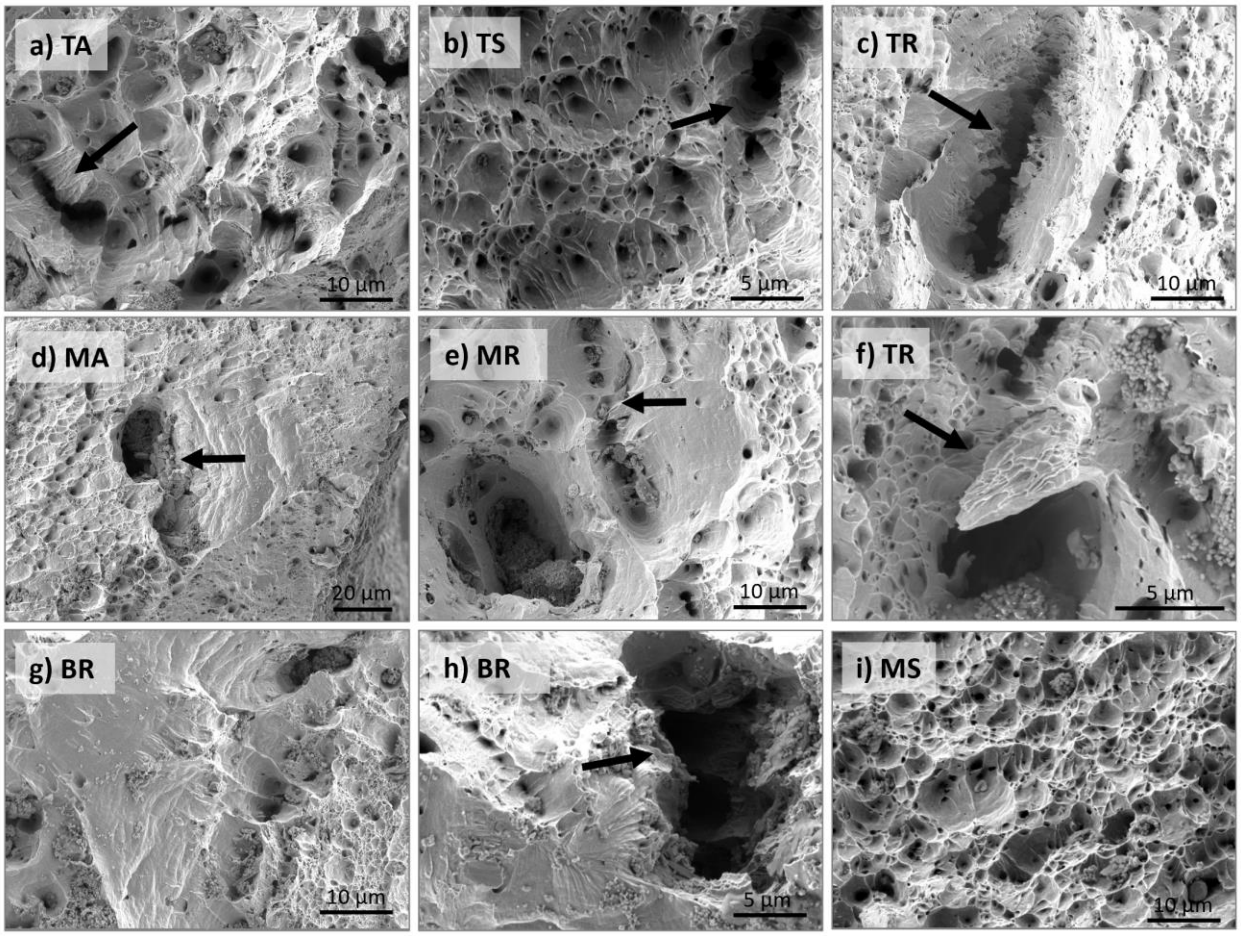

Figure 26. Fracture surface features showing internal cracks, large pores, and cleavage-like spots. "MS"-condition image (i) represents typical the ductile fracture for comparison. Note magnification varies for some images; "TR"-condition is shown twice.

3.3.3 Cracking and fracture events at the gauges portion of the tested specimens

Figure 27 illustrates the condition of the specimen gauge sections following the tensile tests and subsequent fracture. Typically, discerning both the necking and the fracture regions is easy. Intriguingly, the majority of the specimens indicate localized fracture along their edges, highlighted at specific locations by black arrows. These locations seem to be randomly distributed; they do not align into a regular zigzag or any ordered pattern, which would be characteristic of conventional strain-induced shear bands. These localized fracture spots are probably associated with helium-rich zones (Figure 9a) possibly generated in the BM production and compromised grain boundaries.

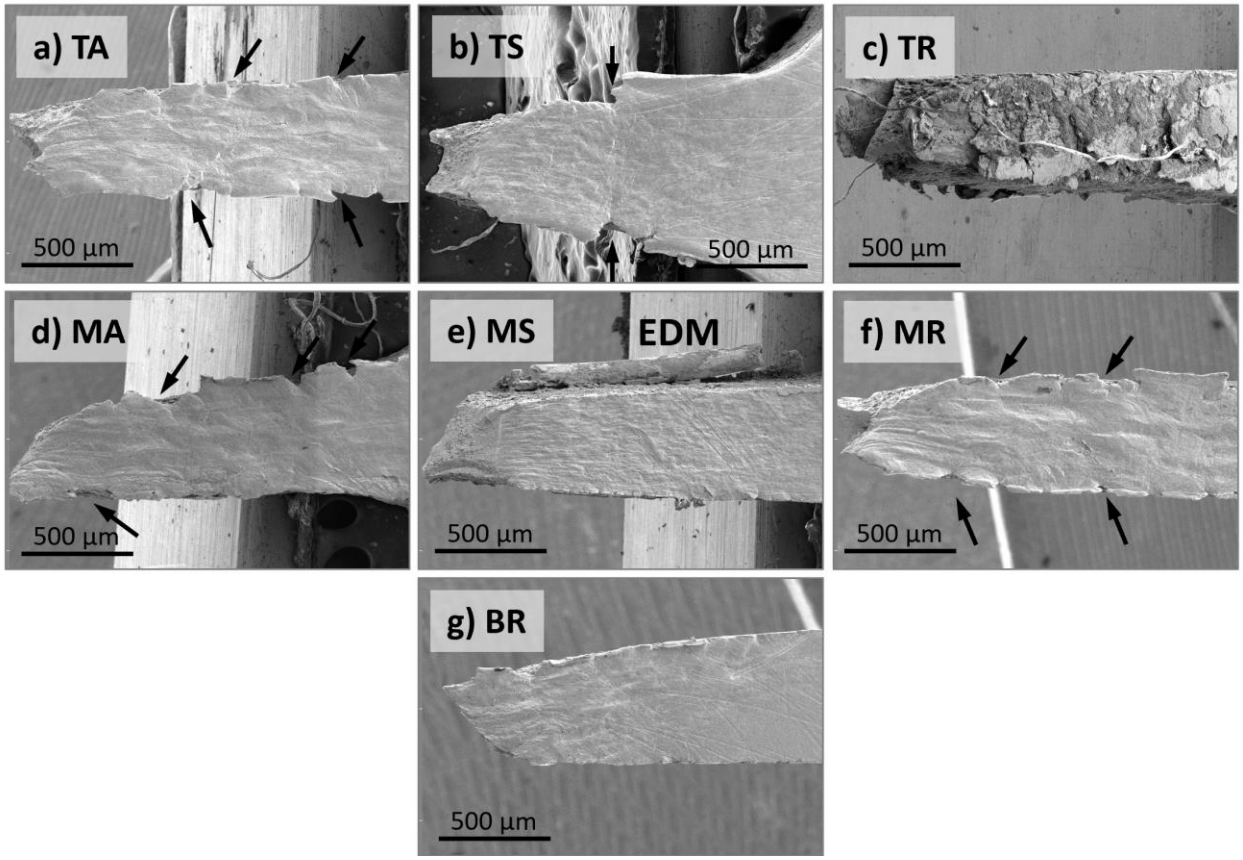

Figure 27. Gauge portions of the tensile specimens after mechanical testing and fracture. Black arrows mark local fracture events (mostly along the gauge edges); the "EDM"-label marks the separation and peeling-off of the EDM-induced layer. Note pronounced delayering at the surface of the TR specimen (c). Material condition IDs are given in Figure 12 and Table 2, pretest specimen geometry is shown in Figure 11.

The presence of these localized fracture spots aligns with the generally erratic pattern of strain localization, as unveiled by DIC analysis (Section 3.2). Notably, both the MS and BR specimens visually exhibited no such fracture spots, likely indicating the lack of helium-rich regions.

By contrast, The TR specimen exhibited an unexpectedly poor surface quality, manifesting multiple crack formations and delamination effects, as shown in Figure 27c. To prevent the formation of debris and dislodged particles, cleaning was executed with extreme care, but some paint residue was deposited within several cracks. Although multiple cracking typically indicates premature fracture and diminished engineering ductility, the ductility for this specimen remains high, as detailed in Table 3: the total elongation value surpasses 40%. Further investigation is required to elucidate this unexpected behavior. Deformation mode may change with material volume and dimension. Actual welded component might be much more bulk, and its deformation mode and failure may not the same as observed in the small specimen.

Figure 28 shows several examples of the fracture events along the gauge. The specific appearance of these areas indicates strong variations in the material conditions. Generally ductile material (slightly deformed austenite in TMAZ) contains specific brittle "clusters" or "kernels," easily fracturing in a brittle way.

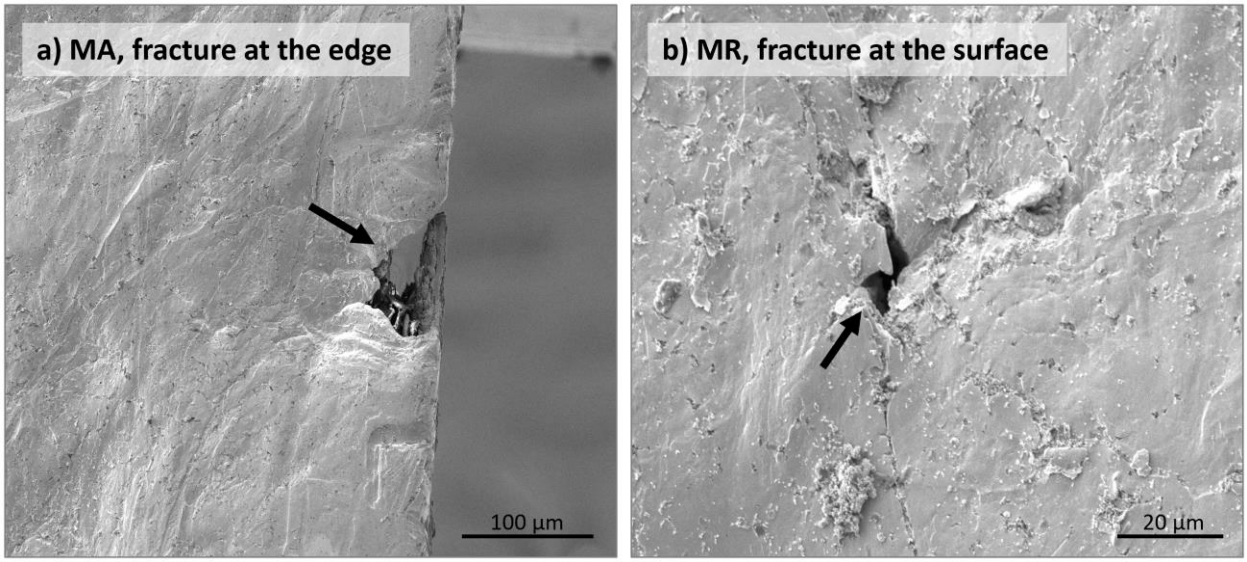

Figure 28. Examples of localized fracture at the specimen gauges. (a) The MA specimen, fracture at the specimen edge. (b) The MR specimen, fracture at the specimen surface, also note a thin wire-like crack. Tensile direction is vertical in this Figure.

Figure 29 shows additional images of the TR specimen, taken from a different specimen half. The figure shows a striking overlapping of pronounced ductility and ductile fracture (also shown in Figure 24 and Figure 25) and multiple delamination and, probably, cleavage processes. Such phenomena could be expected for composite materials, combining ductile/soft and brittle/hard phases or alloy components. In situ tests with an identical specimen should be performed to investigate the phenomenon in more detail.

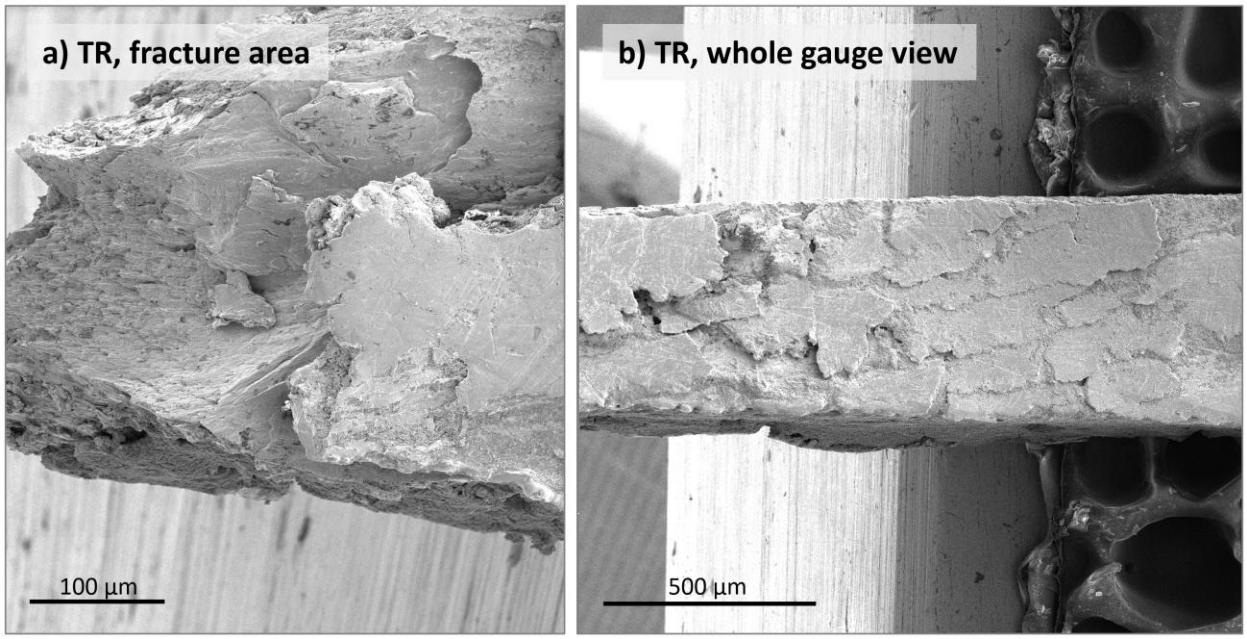

Figure 29. Delayering and multiple cracks at the surface of the TR specimen. This phenomenon is difficult to fully explain now.

4. CONCLUSIONS AND FUTURE WORK

The present work describes experimental results on the microhardness distributions and tensile performance of the friction stir weld made on neutron-irradiated austenitic 304L SS with approximately 10 appm helium. The report evaluates microhardness, tensile curves, tensile properties, and strain distributions in the SZ, TMAZ, and HAZ of the friction stir welds with helium, as well as the effects of the FSW and helium-induced damage on friction stir weld specimen mechanical behaviors.

The grain size dominated the hardness in the SZ zone, higher than BM hardness were obtained in an area close to the weld top surface and at the SZ root, where small grains and superfine grains were observed. Because of FSW thermal and mechanical effects, hardness values in the TMAZ and HAZ were lower than that of the BM.

Tensile tests on miniature tensile specimens extracted from the SZ, SZ root, and TMAZ/HAZ exhibited very good strength and elongation, comparable or higher than ASTM A240/A240M minimum requirements for wrought 304L SS, respectively. Therefore, helium-induced damage (helium bubbles, helium bubbles chains, and a few microcracks presented in the SZ, TMAZ, and HAZ) after FSW did not catastrophically degrade the friction stir weld strength and ductility.

DIC was used to obtain tensile strain distributions of irradiated 304L SS friction stir weld specimens at different metallurgical zones. When tensile stresses were between the YS and UTS, SZ specimens showed uniform strain distribution, SZ root specimen demonstrated early strain localization, and TMAZ/HAZ specimens exhibited multiple strain bands. Those local strain behaviors were related to FSW tool design, FSW thermal and mechanical histories, irradiation, and/or helium evolution during FSW. Further studies are needed to identify mechanisms of the strain band development in the TMAZ/HAZ specimens.

Fractography analysis showed mostly ductile fracture with some brittle areas, likely related to the helium-rich spots. From the BM observation, such helium enriched spots might be produced artificially in the BM production but needs further characterization to determine. Helium-rich spots led to localized fracture effects along the specimen edges and probably in the bulk. Helium-related issues were the most pronounced in the TR specimen, leading to delamination effects.

Although the results mentioned and the data provided are believed to be accurate, more work is necessary to understand, quantify, and explain the observed features and peculiarities and compare them with the literature. The work conducted herein, the selected experimental tools and approaches, and the amount of data obtained all were a result of a compromise between scientific and practical importance and available funds.

Future works of this study include helium-induced damages further characterization, such as in situ test and transmission electron microscopy characterizations, TMAZ/HAZ specimen strain bands and fracture mechanism investigation, and friction stir weld re-irradiation and characterization.

Although more work is necessary, the obtained results show limited helium-induced degradation in the friction stir weldments and their good mechanical performance compared with the conventional welding techniques. FSW is therefore a very promising technological approach for repair welding materials with high helium content.

ACKNOWLEDGMENTS

The research was sponsored by the US Department of Energy, Office of Nuclear Energy, Light Water Reactor Sustainability Program Materials Research Pathway, under contract DE-AC05-00OR22725 with UT Battelle LLC/ORNL, with collaboration from Electric Power Research Institute (EPRI).

It is important to acknowledge the people and teams who worked on the weldment production, irradiated specimen transportation, handling, and preparation including ORNL's REDC, IMET, and LAMDA facilities, ORNL's Materials Joining group, and EPRI. We would like to thank A. Smith, K. Kinney, C. Scott White, M. Delph, C. Morris, T. Davis, R. Bowman, S. Thurman, T. Muth, P. Tedder, S. Curlin, T. Dixon, M. McAlister, Z. Feng, J. Chen, R. Miller, S. Clark, K. Leonard, Jon Tatman, Greg Frederick, and many others. The authors acknowledge Yiyu Wang and TS Byun for the technical review of this report.

REFERENCES

[1] W. Kanne Jr, Remote reactor repair: GTA weld cracking caused by entrapped helium, Weld. J. 67 (1988) 33–39.

[2] K. Asano, S. Nishimura, Y. Saito, H. Sakamoto, Y. Yamada, T. Kato, T. Hashimoto, Weldability of neutron irradiated austenitic stainless steels, J. Nucl. Mater. 264 (1999) 1–9.

[3] S. Kawano, F. Kano, C. Kinoshita, A. Hasegawa, K. Abe, Effect of weld thermal cycle, stress and helium content on helium bubble formation in stainless steels, J. Nucl. Mater. 307 (2002) 327–330.

[4] R.S. Mishra, Z. Ma, Friction stir welding and processing, Mater. Sci. Eng. R Rep. 50 (2005) 1–78.

[5] D. Lohwasser, Z. Chen, Friction stir welding: From basics to applications, Elsevier, 2009.

[6] W. Tang, M. Gussev, Z. Feng, B. Gibson, R. Miller, J. Chen, S. Clark, K. Leonard, J. Tatman, B. Sutton, others, Friction Stir Welding and Preliminary Characterization of Irradiated 304 Stainless Steel, in: ASME 2019 Press. Vessels Pip. Conf., American Society of Mechanical Engineers Digital Collection, 2019.

[7] B.T. Gibson, W. Tang, A.G. Peterson, Z. Feng, G.J. Frederick, Evaluating the potential for remote in-process monitoring of tool wear in friction stir welding of stainless steel, J. Manuf. Sci. Eng. 140 (2018).

[8] Canaday, Clinton T., Matthew A. Moore, Wei Tang, and Anthony P. Reynolds. Through thickness property variations in a thick plate AA7050 friction stir welded joint. Materials Science and Engineering, A 559 (2013): 678-682.

[9] Pilchak, A. L., W. Tang, H. Sahiner, Anthony P. Reynolds, and J. C. Williams. Microstructure evolution during friction stir welding of mill-annealed Ti-6Al-4V. Metallurgical and Materials Transactions A, 42 (2011): 745-762.

[10] Reynolds, Anthony P., Wei Tang, Thomas Gnaupel-Herold, and et H. Prask. Structure, properties, and residual stress of 304L stainless steel friction stir welds. Scripta Materialia, 48(2003): 1289-1294.

[11] Reynolds, Anthony P., W. Tang, M. Posada, and J. DeLoach. Friction stir welding of DH36 steel. Science and technology of welding and joining, 8(2003): 455-460.

[12] Tang, Wei, Jian Chen, Xinghua Yu, David A. Frederick, and Zhili Feng. Heat input and post weld heat treatment effects on reduced-activation ferritic/martensitic steel friction stir welds. Friction stir welding and processing VIII (2016): 83-87.

[13] Thomas, W. M., C. S. Wiesner, D. J. Marks, and D. G. Staines. Conventional and bobbin friction stir welding of 12% chromium alloy steel using composite refractory tool materials." Science and Technology of Welding and Joining, 14(2009): 247-253.

[14] W. Tang, J. Chen, B.T. Gibson, R.G. Miller, S.R. Clark, M.C. Vance, Z. Feng, K.J. Leonard, J.K. Tatman, B. Sutton, others, Advanced welding technology development for nuclear reactor repair, Oak Ridge National Laboratory, Oak Ridge, TN (United States), 2018.

[15] Z. Feng, R.G. Miller, J. Chen, W. Tang, S.R. Clark, B.T. Gibson, M.C. Vance, G. Frederick, J.K. Tatman, B.J. Sutton, Report on the Progress of Weld Development of Irradiated Materials at the Oak Ridge National Laboratory, Oak Ridge National Laboratory, Oak Ridge, TN (United States), 2018.

[16] Zhili Feng, Wei Tang, Roger Miller, Jian Chen, Scarlett Clark, Brian Gibson, Mark Vance, Gregory Frederick, Jonathan Tatman, Benjamin Sutton, Complete Report on Development of Weld Repair Technology. Oak Ridge National Laboratory, ORNL/SPR-2018/1035, Oak Ridge, TN, 2018.

[17] M. N. Gussev, W. Tang, N. Bibhanshu, T. M. Rosseel, Microstructure and Mechanical Performance of the Friction Stir WeldsMadeon Neutron-Irradiated Steel with Helium. Oak Ridge National Laboratory, ORNL/TM-2021/2079, Oak Ridge, TN, 2021.

[18] Zhili Feng, Nesrin Cetiner, Roger Miller, Greg Frederick, Completion of the first batch of irradiation experiments to produce helium-containing SS304 samples for use in development of weld repair techniques. Oak Ridge National Laboratory, M3LW-14OR0406014, Oak Ridge, TN, 2014.

[19] C. Gunter, M.P. Miles, F.C. Liu, T.W Nelson, Solid state crack repair by friction stir processing in 304L stainless steel, Journal of Materials Science & Technology 34 (2018) 140–147.

[20] ASTM A240/A240M-20a, Standard Specification for Chromium and Chromium-Nickel Stainless Steel Plate, Sheet, and Strip for Pressure Vessels and for General Applications. ASTM International, 2020.

[21] W. Tang, M. Gussev, X. Chen, T. M. Rosseel, Friction stir welding – an advanced approach to repair nuclear power plant components. 20th International Conference on Environmental Degradation of Materials in Nuclear Power Systems – Water reactors. July 17 – 20, 2022, Snowmass Village, CO.